Impact of the carbon cycle on the development of a Snowball Earth

Master-Thesis

submitting date: April 10, 2014

Climate Physics MSc
Faculty of Mathematics and Natural Sciences
Christian-Albrechts-Universität zu Kiel

Submitted by: Tronje Peer Kemena (834551)
First supervisor: Prof. Dr. Andreas Oschlies
Second supervisor: Dr. David Keller

Abstract

This study investigates the impact of the carbon cycle on the development of a modern Snowball Earth with the University of Victoria (UVic) earth system climate model including a modern present day topography. A Snowball Earth is initiated by a fixed reduction of the incoming solar radiation. The bifurcation point for a model run with constant preindustrial carbon dioxide concentrations lays between 91% and 94% of the present day incoming solar radiation (PDISR),which is similar to other modern-day Snowball Earth studies.

The land and ocean carbon cycle of the model run with 91% PDSIR has the strongest impact on the development of a Snowball Earth. The carbon dioxide concentration of this model run varies from 232 to 532 ppmv and the changes in the respective greenhouse forcing ranges from -1 to 3.4 W m^{-2} relative to preindustrial forcing. The carbon cycle delays a Snowball Earth state by almost 1000 years in comparison to the model run with fixed atmospheric carbon dioxide concentration.

Additional model configurations are designed with 91% PDSIR to analyze the land and ocean carbon cycle independent from each other. The accumulation of carbon in the land soil dominates the global carbon flux during the first years of the simulation, because of colder surface and soil temperatures. The colder temperatures reduce the global soil respiration and improve the conditions for vegetation in tropical and subtropical regions. Changes in the ocean circulation and convection at the sea ice edges are also responsible for the upwelling of carbon rich waters from the deep ocean. All simulations (with 91% PDSIR) experience a warm phase as the sea ice reaches the tropical ocean. During this warm phase a weaker and shallower ocean circulation can be observed. The warming and melting of sea ice at the ice edges increases the vertical density gradient of the ocean. Strong vertical density gradient then suppresses the upwelling of the carbon rich waters. At the beginning of the warm phase high soil temperatures are responsible for a strong carbon dioxide flux from the land to the atmosphere. These high atmospheric carbon dioxide concentrations allow the warm phase to persist for more than 1000 years. The removal of carbon dioxide by the biological pump in the ocean is responsible for the reduction in atmospheric carbon dioxide and for the final development of a Snowball Earth.

However, since the UVic model has a simple energy-moisture balance atmosphere component it cannot simulate some important feedbacks. Since these atmospheric feedbacks are important for controlling sea ice expansion and the poleward atmospheric heat transport (Voigt and Marotzke, 2009; Yang et al., 2012b), further investigations are necessary to reduce the uncertainties involved in the transition to a Snowball Earth state.

Zusammenfassung

Die vorgelegte Studie untersucht den Einfluss des Kohlenstoffkreislaufs auf die Entwicklung einer heutigen Schneeball Erde mittels des University of Victoria (UVic) Erdsystem Klimamodell mit gegenwärtiger Topografie. Eine Reduktion der Sonneneinstrahlung initiiert die Entstehung der Schneeball Erde. Der Bifurkationspunkt für einen Modelllauf mit vorindustrieller Kohlenstoffdioxid Konzentration liegt zwischen 91% und 94% bezogen auf die mittlere Sonneneinstrahlung der Gegenwart (PDISR). Diese Ergebnisse sind vergleichbar zu den Ergebnissen anderer wissenschaftlicher Untersuchungen.

Der Land und Ozean Kohlenstoffkreislauf für den Modelllauf mit 94% PDSIR hat den grössten Einfluss auf die Entwicklung einer Schneeball Erde. Die Kohlenstoffdioxid Konzentration dieses Modelllaufs variiert von 232 bis 532 ppmv und der entsprechende Strahlungsantrieb variiert von -1 bis 3.4 W m^{-2}, relativ zum vorindustriellen Referenzwert. Der Einfluss des Kohlenstoffkreislaufs zögert die Entstehung der Schneeball Erde um fast 1000 Jahre hinaus im Vergleich zu dem entsprechenden Modelllauf mit konstanter atmosphärischer Kohlenstoffdioxid Konzentration.

Weitere Modellkonfigurationen mit 91% PDSIR wurden aufgesetzt um den Land und Ozean Kohlenstoffkreislauf unabhängig voneinander untersuchen zu können. Die Zunahme von Kohlenstoff im Erdboden dominiert die globalen Änderung in den Kohlenstoffreservoirs während der ersten Jahre, aufgrund der niedrigeren Oberflächen- und Bodentemperaturen. Niedrige Temperaturen verringern die globale Bodenrespiration und verbessern die Bedingungen für Vegetation in tropischen und subtropischen Regionen. Änderungen in der Ozeanzirkulation und in der Konvektion an den Seeeisrändern sind für den Auftrieb von kohlenstoffreichem Wasser aus dem tiefen Ozean verantwortlich. In allen Simulationen (mit 91% PDSIR) entwickelt sich eine Warmphase wenn das Seeeis den tropischen Ozean erreicht. Während dieser Warmphase ist eine schwächere und flachere Ozeanzirkulation zu beobachten. Die Erwärmung und das schmelzende Seeeis an den Seeisrändern verstärken den vertikalen Dichtegradienten im Ozean. Der hohe vertikale Dichtegradient unterdrückt den weiteren Auftrieb von kohlenstoffreichem Wasser. Am Anfang der Warmphase sind hohe Bodentemperaturen für einen erhöhten Kohlendioxidfluss vom Land in die Atmosphäre verantwortlich. Der hohe Kohlendioxidgehalt in der Atmosphäre ermöglicht ein Andauern der Warmphase für mehr als 1000 Jahre. Die Kohlendioxid Aufnahme des Ozeans durch die biologische Pumpe ist für die abschliessende Entwicklung der Schneeball Erde verantwortlich.

Weil das UVic Modell ein simples Energie-Feuchtigkeits-Balance Atmosphären Modell hat, können einige wichtigen Feedbacks nicht simuliert werden. Diese atmosphärischen Feedbacks können die Ausdehnung des Seeeises und den atmosphärischen Wärmetransports steuern und beeinflussen (Voigt and Marotzke, 2009; Yang et al., 2012b). Daher sind weitergehende Untersuchungen notwendig um Unsicherheiten zu reduzieren, die während einer Schneeball Erde Simulation entstehen können.

Contents

1 Introduction

The term Snowball Earth was coined by Joe Kirschvink, who first proposed the hypothesis that such a Snowball Earth state occurred during the Neoproterozoic era (Kirschvink, 1992). Since this day many model studies have investigated the development of a Snowball Earth. Some of them are presented below.

With a coupled atmosphere-ocean general circulation model Voigt et al. (2011) showed that a reduction of only 4% to 4.5% in the solar constant (SC) is already enough to trigger the development of a Snowball Earth under Neoproterozoic conditions. To trigger a Snowball Earth under present-day climate conditions (in the following called Snowball Earth) a reduction between 6% and 9% in the SC is required (Voigt and Marotzke, 2009). Reducing the incoming solar radiation is one typical method to initiate a Snowball Earth. Another method is to reduce the greenhouse effect for example by reducing the atmospheric carbon dioxide concentration. Yang et al. (2012a) combined both methods and showed that as well a reduction of 10% to 10.5% in the SC at preindustrial carbon dioxide concentrations as a reduction of 6% in the SC and an absolute carbon dioxide concentration of 17.5 ppmv can produce similar results initiating a Snowball Earth. Voigt et al. (2011) evaluated model runs with an increased carbon dioxide concentration and showed that this can decelerate sea ice expansion during a Snowball Earth development. When a Snowball Earth state is reached, the climate sensitivity is much lower than during the development of a Snowball Earth and deglaciating requires a high amount of atmospheric carbon dioxide (Lewis et al., 2006; Pierrehumbert, 2005). The reduction in sea ice albedo due to the accumulation of dust can allow deglaciation with a much lower carbon dioxide concentration (Goodman and Strom, 2013).

Typically it is distinguished between two different Snowball Earth states: The soft Snowball Earth and the hard Snowball Earth. The hard Snowball Earth (called in general Snowball Earth) describes an Earth with complete sea ice and snow cover and the soft Snowball Earth an almost but not complete sea ice and snow covered earth. A soft Snowball Earth would be more likely to provide regions with suitable conditions for biological organisms or vegetation. Lewis et al. (2007) investigated Neoproterozoic Snowball Earth simulations with the University of Victoria (UVic) model, a model with prescribed wind fields. They found out that it is only possible to simulate a soft Snowball Earth with a non dynamic sea ice model. They also observed a large influence of the wind stress field on the dynamics of the sea ice. In contrast to this Yang et al. (2012a) used the Community Climate System Model (CCSM3) which contains a dynamic sea ice model and simulated a soft Snowball Earth with 76% sea ice cover with sea ice margins extending to 10°S(N). They pointed out that the initiation of a Snowball Earth is very sensitive to the chosen values of the snow and sea ice albedo. Voigt and Abbot (2012) stated that different sea ice dynamics schemes can be just as similar important as the differences in

the sea ice albedo, because sea ice dynamics are responsible for the destabilization of the tropical sea ice margins. An intensification of the Hadley Cell can be observed during the development of a Snowball Earth (Voigt and Marotzke, 2009; Yang et al., 2012b). This intensification and the adjustment of the wind-driven ocean circulation can inhibit the expansion of sea ice into the tropics, thus playing an important role in the development of a Snowball Earth (Yang et al., 2012b).

Most other studies investigated the influence of the greenhouse gas forcing on the development of a modern Snowball Earth only with fixed carbon dioxide concentrations, so the effects of the carbon cycle are unknown. Therefore the here presented study offers a new approach. Snowball Earth is simulated with dynamically varying carbon dioxide concentrations, including a marine and land carbon cycle and the effects of the oceanic solubility pump. The UVic model version, which is available at the GEOMAR - Helmholtz-Zentrum für Ozeanforschung Kiel, is very useful for this approach, because it already includes the land and marine carbon cycle. Furthermore the computation time for an UVic model run is relatively short, which makes it possible to investigate multiple model runs with different carbon cycle configurations.

A Snowball Earth simulation describes an extreme climate change, which is a challenge to every earth system model. In the UVic model parametrizations are used to simplify different processes. These parametrizations are only valid under certain conditions. Therefore chapter 2 describes not only the different modules of the GEOMAR UVic version but also modifications to the atmospheric model of intermediate complexity. Then in chapter 3.1 a comparison between UVic model runs and the model runs performed by Voigt and Marotzke (2009) is conducted. Chapter 3.2.1 includes preliminary work to determine the best forcing to induce a Snowball Earth. Therefore model runs are carried out with reduced incoming solar radiation ranging from 6 - 50% with and without the influence of the carbon cycle. For all further investigations a model configuration with a 9% reduction of incoming solar radiation was chosen, because it shows the largest influence of the carbon cycle on the expansion of sea ice, delaying a Snowball Earth state for up to 1000 years. To workout the general response of the circulation and of the atmospheric and oceanic energy balance, in chapter 3.2.2 a model run with constant carbon dioxide concentration is analyzed. In the following chapters variable atmospheric carbon dioxide concentrations are allowed, to determine the effect of the solubility pump (chapter 3.2.3), the marine ecosystem (chapter 3.2.4) and the land vegetation (chapter 3.2.5). A brief description of the effects of an alternative prescribed wind field can be found in chapter 3.2.6. Chapter 3.3 presents the conclusions that are drawn from comparisons to results with other papers and their findings, this chapter also includes suggestion for further investigations. The summary can be found in chapter 4.

2 Model and Methods

2.1 General Model Description

The University of Victoria (UVic) Earth System Climate Model (Weaver et al., 2001) at version (2.9) is used for this investigation with a present day topography. This model consists of a 3-D ocean general circulation model with 19 depth levels and with a coarse grid resolution of 3.6° in zonal and 1.8° in meridional direction. The ocean is coupled to a thermodynamic / dynamic sea ice model and a reduced-complexity energy-moisture balance atmosphere model. The UVic model is evaluated under present day, global warming and glacial climate conditions and compared to other modeling studies (Eby et al., 2009; Weaver et al., 2001). Comparisons to the Climate: Long range Investigation, Mapping, and Prediction (CLIMAP) showed generally cooler last glacial maximum surface air temperatures, but not as cold as some other reconstructions (Weaver et al., 2001). Eby et al. (2013) provide a detailed intercomparision of earth system models of intermediate complexity also including the UVic model. To describe the carbon cycle an improved marine biogeochemical ecosystem model from Keller et al. (2012) and a dynamic vegetation model from Meissner et al. (2003) is used. The dynamic vegetation model TRIFFID (Top-down Representation of Interactive Foliage and Flora Including Dynamics) together with the land surface MOSES (Met Office Surface Exchange Scheme) is coupled to an atmospheric moisture balance model.

Atmospheric advection, diffusion and wind stress are computed from prescribed seasonal varying wind fields derived from observations and reanalysis data. The atmospheric model is not able to represent cloud processes and their influence on the albedo, therefore the atmospheric albedo is also prescribed as seasonal data. The current model code provides a parametrization of wind stress anomalies. However, preliminary model runs revealed unrealistic large wind velocities during Snowball Earth simulations, therefore this parametrization is not implemented. Simulated precipitation occurs, if relative humidity exceeds 85%. Liquid precipitation over land directly returns back to the corresponding ocean basins. Snow can accumulate at land and changes the albedo slightly with increasing depth reaching the maximum snow albedo $\alpha_{snow} = 0.8$ for an average snow depth of 1 m. The vegetation model accounts for the shielding effect on the surface albedo of the different vegetation types. Therefore the models differs between land areas with and without snow cover. In snow covered areas the surface albedo also depends on the leaf area index. The surface albedos for snow-covered land are linearly interpolated between the snow-cover albedo for large leaf area index (LAI) and for zero LAI by a weighting factor as following

$$\alpha_{SC} = \alpha_{SC,max} \cdot \exp(-0.5 \cdot \mathrm{LAI}) + \alpha_{SC,min} \cdot \Big(1 - \exp(-0.5 \cdot \mathrm{LAI})\Big) \tag{1}$$

with the different maximum and minimum surface albedo values given in table 1. The surface albedo for snow-free sea ice is set to 0.75.

Table 1: Different surface albedos depending on the leaf area index (LAI) and the snow cover

land cover	Broadleaf trees	Needleleaf trees	C_3 grasses	C_4 grasses	shrubs
Snow-covered albedo $\alpha_{SC,max}$ for large LAI	0.35	0.35	0.60	0.60	0.40
Snow-covered albedo $\alpha_{SC,min}$ for zero LAI	0.65	0.65	0.80	0.80	0.80
Snow-free albedo α_{SF} for large LAI	0.16	0.16	0.20	0.20	0.20

The sea ice model also allows for snow on the sea ice and the snow is converted to sea ice, if the water line reaches the snow. Sea ice thickness also influences the ocean surface pressure field and with this the geostrophic surface currents. Preliminary model runs with a Snowball Earth scenario showed that between to adjacent grid cells sea ice thickness differences of more than 50 m can occur, leading to unrealistic surface geostrophic velocities of up to 10 m/s. Under these conditions the model crashes. A bug fix in a coming model release would be necessary to solve this problem. To avoid this problem the maximum sea ice thickness is reduced to 10 m and the time step for the baroclinic velocity computation is reduced to 45 seconds.

The land vegetation model (Meissner et al., 2003) is based on the Top-down Representation of Interactive Foliage and Flora Including Dynamics (TRIFFID) model (Cox, 2001). TRIFFID defines the state of the terrestrial biosphere in terms of soil carbon and the structure and coverage of five plant functional types: broadleaf tree, needleleaf tree, C3 grass, C4 grass and shrub. Land-atmosphere fluxes, runoff and carbon fluxes are calculated within MOSES every 6 hours and passed then to the atmospheric and ocean model every 2.5 days.

The marine biogeochemical ecosystem model is based on a Nutrient Phytoplankton Zooplankton Detritus (NPZD) model and includes improvements in describing the light and iron limitations for phytoplankton and a more realistic zooplankton growth and grazing model (Keller et al., 2012). The current model version also includes an anisotropic viscosity scheme in the tropics improving the representation of equatorial currents (Getzlaff and Dietze, 2013) and an increased vertical mixing parameter to better represent the southern ocean deep water formation. The anisotropic viscosity scheme and the increased

vertical mixing parameter are included in the spin up runs, but turned off in final runs, because they are probably not applicable for the Snowball Earth scenario. Preliminary model runs showed that the expansion of the sea ice is temporary or completely inhibited at 20 °N/S for an activated anisotropic viscosity scheme in contrast to model runs with standard viscosity. At 20 °N/S strong meridional pressure gradients appear for model runs with an anisotropic viscosity scheme.

2.2 Limitations of the Atmospheric Energy Model

To model the atmosphere Weaver et al. (2001) implemented a modified version of the energy-moisture balance model from Fanning and Weaver (1996) in the UVic model. Due to the simplistic nature of this atmospheric model component, several parameterizations had to be modified to allow for a Snowball Earth to be simulated. The first modification is to the energy balance equation which will be described in the following. The energy balance equation of the one layer atmospheric model (here with coupling to the ocean, figure 1) is given by

$$\rho_a h_t c_{pa} \frac{\partial T_a}{\partial t} = Q_T + Q_{SW} C_A + Q_{LH} + Q_{LW} + Q_{SH} - Q_{PLW} \tag{2}$$

where the term on the left-hand side of the equation describes from an eulerian view the change in heat storage in the atmospheric air column with the corresponding air temperature T_a, h_t = 8.4km the scale height, ρ_a = 1.25kg m^{-3} the density of air and c_{pa} = 1004 J kg^{-1} K^{-1} the specific heat of air. The terms on the right-hand side of (2) are the different heat fluxes. Q_T is the transport of heat in the horizontal due to advection, Q_{LH} the latent and Q_{SH} the sensible heat flux between ocean and atmosphere, $Q_{SW} \cdot C_A$ the atmospheric passing shortwave radiation and C_A=0.23 the atmospheric absorption coefficient. The latter parametrizes the absorption due to water vapor, dust, ozone and clouds. The equations for the longwave radiation is split up into two different parts. One describes the longwave flux at the top of the atmosphere (4) and the other the fluxes at the bottom of the atmosphere (3). For the latter the atmosphere and ocean are assumed to be gray body emitters with the heat flux written as

$$Q_{LW} = \epsilon_S \sigma T_S^4 - \epsilon_A \sigma T_a^4 \tag{3}$$

with T_S being the surface temperature and with ϵ_S and ϵ_A being the different emissivities of the surface and the atmosphere.

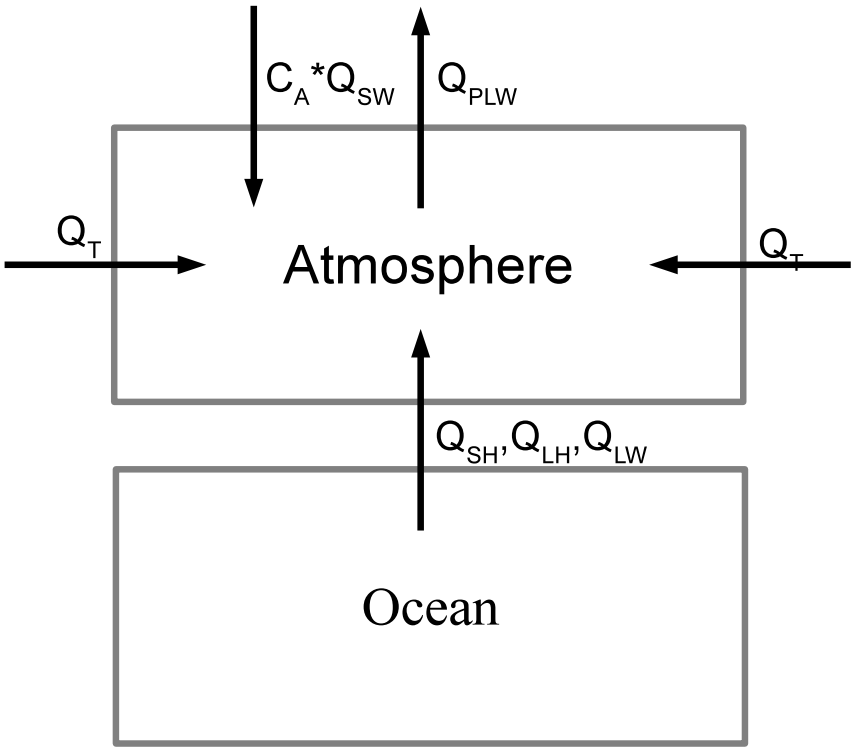

Figure 1: Schematic overview of atmospheric heat fluxes: Q_T advection of heat in the horizontal, Q_{PLW} emitted longwave radiation to the space, $C_A * Q_{SW}$ from the atmosphere absorbed shortwave radiation, Q_{SH} sensible heat flux, Q_{LH} latent heat flux, Q_{LW} longwave radiation balance at the bottom of the atmospheric layer. Arrow directions indicate positive values corresponding to equation (2).

The emitted longwave radiation at the top of the atmosphere depends on several parameters, e.g. the vertical temperature profile, the cloud cover and the concentration of the different greenhouse gases. The UVic model does not take all of these contributing factors into account. The following parametrization for the outgoing planetary longwave radiation into space is included in the current UVic model release

$$\begin{aligned} Q_{PLW} =& c_{00} + c_{01} r + c_{02} r^2 \\ &+ (c_{10} + c_{11} r + c_{12} r^2) T_a \\ &+ (c_{20} + c_{21} r + c_{22} r^2) T_a^2 \\ &+ (c_{30} + c_{31} r + c_{32} r^2) T_a^3 \\ &- \Delta F_{2x} \ln\Big(\frac{C(t)}{C_0}\Big) \end{aligned} \tag{4}$$

with dependences of surface air temperature T_a and relative humidity r with different parametrization coefficients c to model the absorption of longwave radiation due to hy-

drogen oxide. The last line of equation (4) deals with the influence of carbon dioxide, which is explained later. Hydrogen oxide influences the longwave radiation as water vapor, water droplets and as ice in clouds. To model the clear-sky greenhouse effect of H_2O a parametrization from Thompson and Warren (1982) is used with valid temperatures between −118 °C and 57 °C. They optimized the parameters c_{nm}, with n=1, 2, 3 and m=0, 1, 2, by fitting the curve to the results from a full complex radiative transfer model. Equation (4) treats only the clear-sky greenhouse effects and not the effects due to clouds. Weaver et al. (2001) added the term $-\Delta F_{2x} \ln(C(t)/C_0)$ to (4) to model the clear-sky greenhouse effect due to the carbon dioxide concentration. $C(t)/C_0$ is the ratio of the actual atmospheric carbon dioxide concentration in relation to a reference carbon dioxide concentration. In this study the reference level it set to the preindustrial CO_2 concentration of C = 280 ppmv and ΔF_{2x} is set to 5.35W/m^2. At the reference concentration the radiative forcing is by definition zero and a doubling of the concentration is equal to a radiative forcing of 3.71 W/m^2. In figure 2 equation (4) is shown for a carbon dioxide concentration of 560 ppmv. For temperatures below −136 °C the outgoing longwave radiation increases for decreasing surface temperatures. This heat flux would lead to an unrealistic atmospheric cooling.

Pierrehumbert (2005) showed with a general circulation model and a radiation model that under Snowball Earth conditions the clear-sky greenhouse effect decreases. Due to the low temperatures the convection is suppressed and the vertical profile of temperature is approximately an isothermal. This means the radiation temperature at the top of the atmosphere roughly matches the radiation temperature at the surface. On the winter hemisphere in the extra tropics the clear-sky greenhouse effect can even become negative (Pierrehumbert, 2005). The clear-sky greenhouse effect is defined as

$$G = Q_{LW\nearrow} - Q_{PLW} \tag{5}$$

with $Q_{LW\nearrow} = \epsilon_S \sigma T_S^4$ the upward longwave radiation at the surface and the surface emissivity ϵ_s = 0.94, taken from Weaver et al. (2001). Lewis et al. (2006) roughly approximated the decrease in the clear-sky greenhouse effect to model a Snowball Earth scenario with the UVic model. For surface temperatures over 250 K the original parametrization for the clear-sky greenhouse effect is not changed and for temperatures from 250 K to 220 K the clear-sky greenhouse effect is linearly decreased to zero. For this study the approximation from Lewis et al. (2006) is implemented. Figure 2 shows the planetary outgoing longwave radiation, for temperatures below 220 K the heat flux corresponds to the Stefan Boltzmann law with $Q_{PLW} = \epsilon_S \sigma T_S^4$.

The model uses an Euler (or forward) scheme to calculate the finite amount of the heat storage change in the atmosphere during each time step. This forward scheme computes

the new temperature with the flux of the previous time step. Starting at temperatures close to 0 K this can result in temperatures lower than 0 K. The forward scheme is a first order accurate scheme so the error of the model increases with the time increment. To reduce the computational time, the time increment for the atmospheric tracers is chosen to be as large as possible. To avoid temperatures below 0 K a cut off at 0 K is implemented.

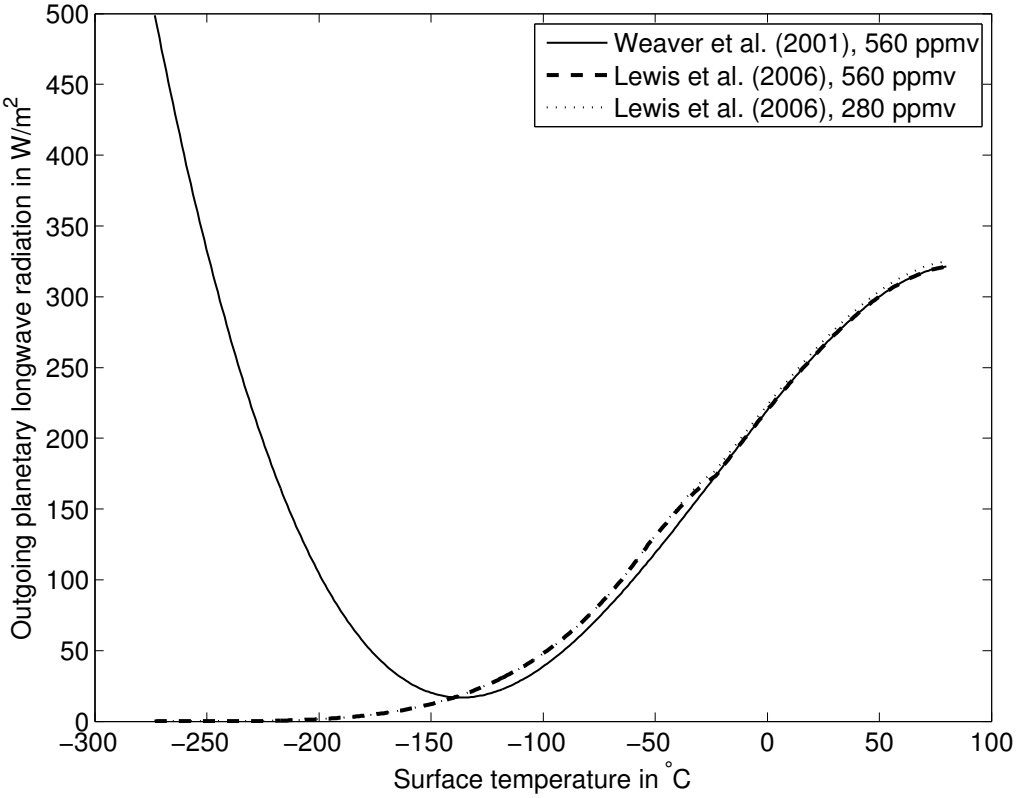

Figure 2: Clear-sky outgoing longwave radiation at the top of the atmospheric layer calculated for a relative humidity r = 0.5, for carbon dioxide concentration of 560 ppmv and 280 ppmv for different approaches. Weaver et al. (2001) approach is given by equation (4).

The Clausius-Claperyon equation describes the relationship between the temperature and the saturation pressure of water vapor e_s. Since there is no analytic solution for this implicit equation, the approximation for the saturation pressure, that is used by the UVic model, is the Magnus-Tetens approximation

$$e_s(T_a) = 6.1094 \cdot exp\Big(\frac{c_1 T_a}{T_a + c_2}\Big) \tag{6}$$

with the constants c_1 = 21.87 and c_2 = 265.5 °C over ice and c_1 = 17.67 and c_2 = 243.5 °C over liquid water. For temperatures below -265.5 °C the sign of the equation (6) switches and the equation outcome results in unrealisticaly large values for the saturation pressure. To prevent this, in this study the saturation pressure is set to zero hPa for temperatures

below 200 K.

2.3 Spin Up Run Configurations

To investigate the influence of the carbon cycle, four different configurations of the UVic model are used (shown in table 2). A 10k years model spin up was done individually for every configuration with a constant preindustrial atmospheric carbon concentration of 280 ppmv.

Table 2: Model configurations for the spin up

Simulation	Vegetation	NPZD
SC1.0	Yes	Yes
SC1.0noNPZD	Yes	No
SC1.0noVeg	No	Yes
SC1.0noVegNPZD	No	No

Applied total solar irradiance SC=1368 Wm^{-2}.
SC1.0 denotes that the incoming solar radiation is set to $1.0 \cdot$ SC.

Table 3 shows annual global values averaged for the last 1000 years of the spin up for different variables. The surface temperature shows a negligible trend of less than 0.02 °C per 1000 years and the heat fluxes into the ocean are small enough that it can be assumed, that the simulation reached its thermodynamic equilibrium. The sea ice area, surface air temperature and surface albedo have similar values among all four spin up runs. The relevant differences are in ocean carbon reservoirs. The ocean total carbon reservoir is up to 3,500 Pg larger for model runs with NPZD model than for model runs without NPZD model. For comparison, the atmosphere has a reservoir of roughly 600 Pg. The deactivation of the NPZD component, without dissolved inorganic carbon values from a individual spin up run, would result in strong ocean to atmosphere carbon fluxes. This would dominate the atmospheric carbon concentration.
The zonal average surface albedo with latitude as the x-axis is shown in figure 3. The NPZD model has no influence on the surface albedo, because there are no feedbacks of the NPZD model on the ocean surface albedo and therefore show now difference to the spin up runs without the NPZD model. In general, north of 40°N spin up runs with vegetation shows higher surface albedos than the spin up runs without vegetation (blue line). At the North Pole the largest difference of 15% occurs and further south between 60 and 75°N a second maximum of 8% occurs. The spin up with vegetation has up to 1.5% smaller surface albedos between 30°N and 40°N. The snow shielding effect of vegetation in the area of the Tibetan Plateau is responsible for these deviations with local differences of up to 36%.

Table 3: Annual global values averaged over the last 1000 years of the spin up.

Variable	SC1.0	SC1.0noNPZD	SC1.0noVeg	SC1.0noVegNPZD
Sea ice cover (%)	6.2	6.2	6.0	6.0
Surface air temperature (°C)	13.3	13.3	13.4	13.4
Trend surface air temperature (°C a^{-1})	$9.1 \cdot 10^{-6}$	$11.5 \cdot 10^{-6}$	$0.8 \cdot 10^{-6}$	$9.3 \cdot 10^{-6}$
Surface upward heat flux, ocean (PW)	$0.1 \cdot 10^{-3}$	$-0.5 \cdot 10^{-3}$	$1.5 \cdot 10^{-3}$	$-3.1 \cdot 10^{-3}$
Ocean and land surface albedo (%)	17.4	17.4	17.3	17.3
Total ocean carbon(Pg)	$38.2 \cdot 10^{3}$	$34.6 \cdot 10^{3}$	$38.5 \cdot 10^{3}$	$34.6 \cdot 10^{3}$
Atmosphere to ocean CO_2 flux (Pg yr^{-1})	$2.5 \cdot 10^{-3}$	$-0.1 \cdot 10^{-3}$	$-2.4 \cdot 10^{-3}$	$-2.8 \cdot 10^{-3}$
Atmosphere to land carbon flux (Pg yr^{-1})	$-1.0 \cdot 10^{-3}$	$-1.0 \cdot 10^{-3}$	-	-

For model run description see table 4.

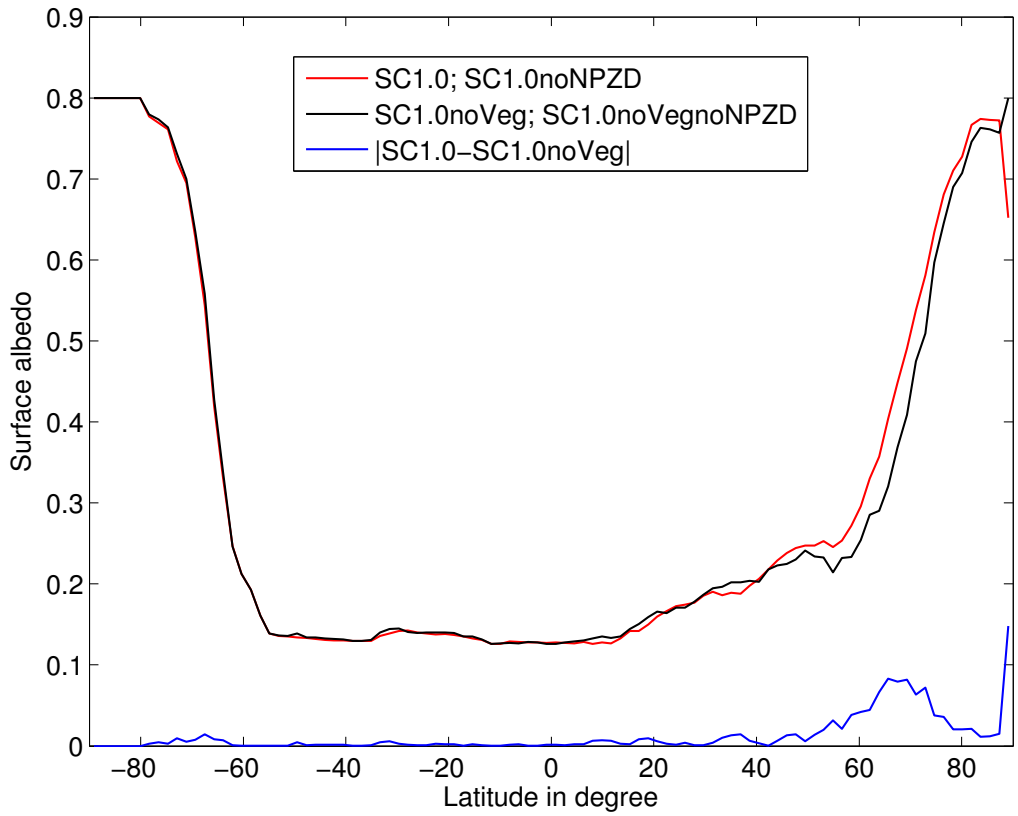

Figure 3: Surface albedo (land and ocean) for the four spin up runs as a zonal and temporal average with the last 1000 years as averaging period. In blue the absolute difference between a model run with and without vegetation is shown.

2.4 Simulation Methods

To simulate a Snowball Earth the incoming solar radiation is reduced to a fixed value for the complete simulation. The applied solar irradiance is given as a factor x.xx of the solar constant SC (1368 Wm^{-2}) denote in the model run name with SCx.xx (see table 4). The transition to a Snowball Earth is defined here in terms of sea ice cover and the Snowball Earth state is defined as an earth with global sea ice cover.

First several model runs were carried out to compare the UVic model to the ECHAM5/MPI-OM model (Voigt and Marotzke, 2009) (chapter 3.1). Voigt and Marotzke (2009) used the ECHAM5/MPI-OM model with ECHAM5 as the atmospheric component. The main part of this chapter is a comparison of the one layer atmospheric model with reduced complexity in UVic against the more complex ECHAM5 model (Voigt and Marotzke, 2009). ECHAM5 is a model of full complexity with 19 vertical levels and provides a detailed radiative transfer model for longwave and shortwave radiation, including the optical properties of clouds. For comparative purposes the configuration of the UVic model without vegetation and without NPZD model is used. Atmospheric carbon dioxide concentration is fixed at the preindustrial level of 280 ppmv, sea ice albedo and snow albedo have the same values of 0.75 and 0.80 respectively, and the incoming solar radiation is reduced to fixed values denoted in the model run notation SCx.xxnoVegNPZD_const_CO2 (see table 4).

To determine the relevance of the carbon cycle on the development of a Snowball Earth, new model runs with the NPZD and vegetation models and with variable atmospheric carbon concentrations were also done (see table 4). Since the model run SC0.91_var_CO2 was the most sensitive to changes in the carbon cycle, several model runs with a reduction of the incoming solar radiation to 91% are carried out to investigate in detail the influence of the carbon cycle. SC0.91noVegNPZD_const_CO2 denotes the reference run with fixed carbon dioxide concentrations. In model run SC0.91noVegNPZD_var_CO2 varying atmospheric carbon dioxide concentration are allowed. In this model run the greenhouse effect due to oceanic absorption or emission of carbon dioxide is investigated. Model run SC0.91noVeg_var_CO2 includes the NPZD model so that the influence of the marine ecosystem can be investigated. The effect of the land carbon cycle can be investigated with the SC0.91noNPZD_var_CO2 model run.

Finally a sensitivity analysis (model run SC0.91_const_CO2_windhalf and C0.91_var_CO2_windhalf) was performed to investigate the influence of wind on the development of a Snowball Earth.

Table 4: Model experiments.

Simulation	CO_2	Vegetation	NPZD	Chapter
SC0.50noVegNPZD_const_CO2	constant	no	no	3.1
SC0.75noVegNPZD_const_CO2	constant	no	no	3.1
SC0.87noVegNPZD_const_CO2	constant	no	no	3.1
SC0.91noVegNPZD_const_CO2	constant	no	no	3.1
SC0.94noVegNPZD_const_CO2	constant	no	no	3.1
SC0.50_var_CO2	variable	yes	yes	3.2.1
SC0.75_var_CO2	variable	yes	yes	3.2.1
SC0.87_var_CO2	variable	yes	yes	3.2.1
SC0.91_var_CO2	variable	yes	yes	3.2.1
SC0.94_var_CO2	variable	yes	yes	3.2.1
SC0.91noVegNPZD_const_CO2	constant	no	no	3.2.2
SC0.91noVegNPZD_var_CO2	variable	no	no	3.2.3
SC0.91noVeg_var_CO2	variable	no	yes	3.2.4
SC0.91noNPZD_var_CO2	variable	yes	no	3.2.5
SC0.91_const_CO2_windhalf	constant	no	no	3.2.6
SC0.91_var_CO2_windhalf	variable	yes	yes	3.2.6

The applied total solar irradiance is given in xx percentage of 1368 Wm^{-2} and denoted in the model run name with SC0.xx.

3 Results and Discussion

3.1 Comparison with Snowball Earth Simulations of the ECHAM5/MPI-OM Model

In this section the UVic model is validated against results of a modern Snowball Earth run from Voigt and Marotzke (2009). Table 5 shows the transition times to reach a modern Snowball Earth. For both models the transition time decreases as incoming solar irradiance is reduced. For a 50% reduction in the solar constant the transition time with UVic is with 27 years, only ten years shorter than the model run with the ECHAM5/MPI-OM model. However, the UVic model reacts much faster to smaller decreases in solar irradiance with the largest difference (187 years) occurring for the SC0.91noVegNPZD_const_CO2 model run.

Table 5: Comparision of Snowball Earth (SE) transition times for the UVic and the ECHAM5/MPI-OM (Voigt and Marotzke, 2009) model.

Simulation	transition time in years UVic	transition time in years ECHAM5/MPI-OM
SC0.50noVegNPZD_const_CO2	27	37
SC0.75noVegNPZD_const_CO2	53	109
SC0.87noVegNPZD_const_CO2	128	285
SC0.91noVegNPZD_const_CO2	295	480
SC0.94noVegNPZD_const_CO2	sea ice line at 10°S/30°N	sea ice line at 40°S/N

The applied total solar irradiance is given in percentage of 1368 Wm^{-2}, carbon dioxide concentration is held fixed at a preindustrial level.

The SC0.91noVegNPZD_const_CO2 model run has two distinguishable phases of fast sea ice expansion (figure 4). The first phase starts at year 110 and stops at year 150 with 60% sea ice cover and the second phase starts at year 280 with 70% sea ice cover and ends in year 295 when a Snowball Earth state is reached. This is in contrast to the corresponding model run from Voigt and Marotzke (2009). In their simulations only one phase of fast sea ice expansion occurred starting at 55% sea ice cover and ending with full sea ice cover (in year 480).

Since a reduction of the solar constant to 94% does not trigger a Snowball Earth, the bifurcation point has to be between 91% and 94%. These results are in accordance with the studies from Voigt and Marotzke (2009).

The sea ice line stops for the SC0.94noVegNPZD_const_CO2 model run not far from the equator at 10°S, but is more distant in the northern hemisphere at 30 °N. Highest ocean surface temperatures occurs at 8 °N. This meridional asymmetry in sea ice does not happen with the ECHAM5/MPI-OM model, where instead the sea ice line stops symmetrically and more poleward at 40 °N/S.

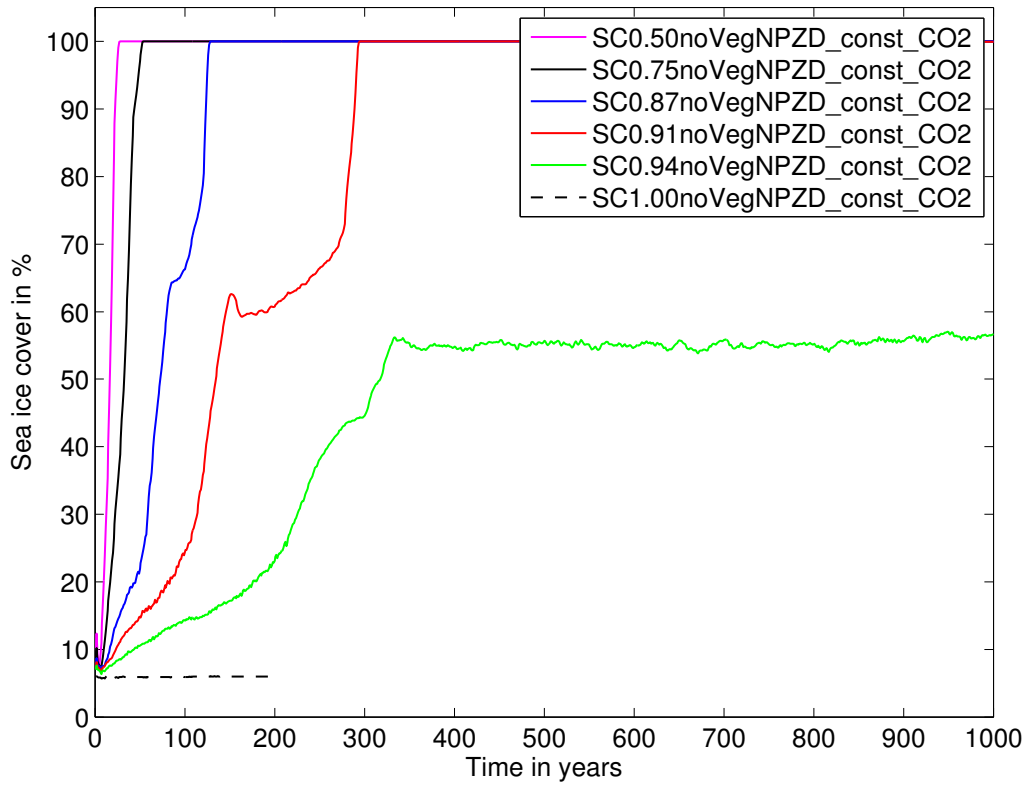

Figure 4: Annual globally averaged sea ice cover in percentage of the global ocean. Solar irradiance is set at the beginning at a fixed value ranging from 50% to 100%.

To investigate the greenhouse effect, Voigt and Marotzke (2009) defined an effective surface emissivity ϵ and distinguished between the clear sky effective surface emissivity $\epsilon_{clearsky}$ and the effect of clouds on the effective surface emissivity ϵ_{clouds} with $\epsilon = \epsilon_{clearsky} + \epsilon_{clouds}$. The UVic model does not include clouds and does not have a parametrication to approximate the effect of clouds on the greenhouse effect. Therefore only $\epsilon_{clearsky}$ is evaluated defined by $\epsilon_{clearsky} = Q_{PLW}/Q_{LW\nearrow}$. Figure 5 shows $\epsilon_{clearsky}$ for the SC0.91noVegNPZD_const_CO2 model run, the initial value of $\epsilon_{clearsky}$ is 71%. For both phases of fast sea ice expansion, ranging from year 110 to 150 and from year 280 to 293, an increase in $\epsilon_{clearsky}$ can be observed, reaching 100% at the Snowball Earth state with a global mean surface temperature of -44 °C. This result is not surprising because $\epsilon_{clearsky}$ is defined to be 100% for temperatures below -53.15 °C (chapter 2.2). The relation to the clear-sky green house effect G (equation 5) is given by $\epsilon_{clearsky} = 1 - G/Q_{LW\nearrow}$. The ECHAM5/MPI-OM model run with a reduction in incoming solar radiation to 91% shows at the beginning a $\epsilon_{clearsky}$ of about 67% and ends at the Snowball Earth state with 90% (figure 2 of Voigt and Marotzke (2009)). Thus, for the ECHAM5/MPI-OM model the greenhouse effect remains stronger for a Snowball Earth climate. In the UVic model the greenhouse effect is reduced to 0 W/m^2 for atmospheric temperatures below -53.15 °C. At these temperatures the ocean should be already covered with sea ice and the difference behavior of both models should not influence the sea ice expansion.

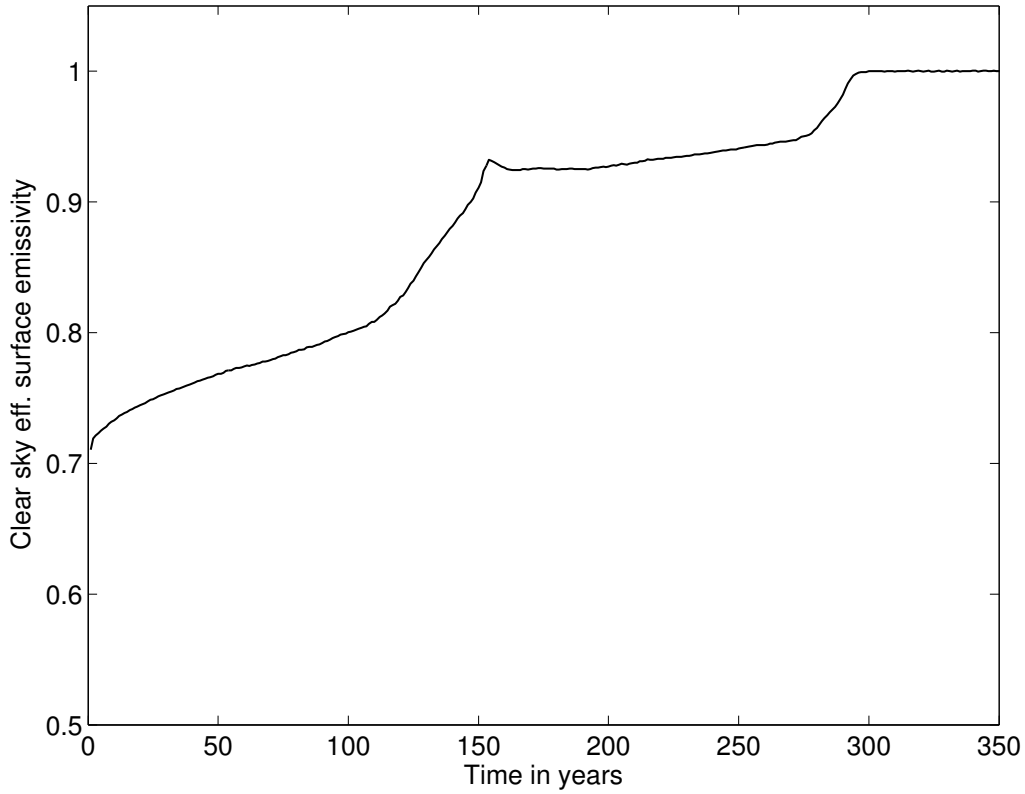

Figure 5: Annual globally averaged clear sky effective surface emissivity $\epsilon_{clearsky}$ for a reduction of the solar irradiance to 91% (SC0.91noVegNPZD_const_CO2 simulation).

The time evolution of different global albedos for the SC0.91noVegNPZD_const_CO2 model run is plotted in figure 6. The planetary albedo α is defined as $\alpha = Q_{SW\nearrow,TOA}/Q_{SW\searrow,TOA}$ with $Q_{SW\nearrow,TOA}$ the upward shortwave radiation and $Q_{SW\searrow,TOA}$ the incoming solar radiation at the top of the atmosphere. The planetary albedo increases from 31% to 58% during the transition to a Snowball Earth. In comparison, the planetary albedo of the respective ECHAM5/MPI-OM model run increases from about 31% to 60% (figure 4 of Voigt and Marotzke (2009)). In the UVic model the planetary albedo depends on the prescribed atmospheric albedo, the surface albedo and the atmospheric absorption coefficient C_A=0.23. The UVic model treats shortwave radiation as described in the following section. Incoming solar radiation can be reflected at the top of the atmosphere, as parametrized by the atmospheric albedo α_{atm}, and downward shortwave radiation at the surface can be reflected, as parametrized by the surface albedo α_{surf}. Shortwave radiation that enters the atmosphere from either direction is absorbed in the atmosphere, as parametrized by the atmospheric absorption coefficient C_A. Therefore the planetary albedo for the UVic model can be computed as:

$$\alpha = \alpha_{atm} + (1 - C_A)^2 \cdot (1 - \alpha_{atm}) \cdot \alpha_{surf} \tag{7}$$

with the global averaged value for the atmospheric albedos α_{atm} = 23%. This value is

comparable to the atmospheric albedo of 23% that can be inferred from the Earth Radiation Budget Experiment (ERBE) Project (Trenberth et al., 2009). Voigt and Marotzke (2009) investigated the effect of clouds on the planetary albedo for a reduction of the solar incoming radiation to 91% and found that planetary albedo increases by 15.5% at year 1 due to clouds. With expanding sea ice cover the effect reduces and reaches 1.5% at full sea ice cover. To compare this with the UVic model the effect was estimated using equation 7 with the global values during Snowball Earth conditions ($\alpha = 0.58$, $\alpha_{surf} = 0.77$, see figure 6). A reduction of the atmospheric albedo α_{atm} from 23% to 0% causes a reduction of 12% in the planetary albedo α, this is comparable to the reduction of 14% in the model run from Voigt and Marotzke (2009) (see above).
The UVic model does not include the effect of changing atmospheric albedo. Only the effect of changing surface albedo is included in the UVic model, therefore it is remarkable that for both model runs (with the ECHAM5/MPI-OM model and the UVic model) the planetary albedo reaches values of around 60% for Snowball Earth conditions.

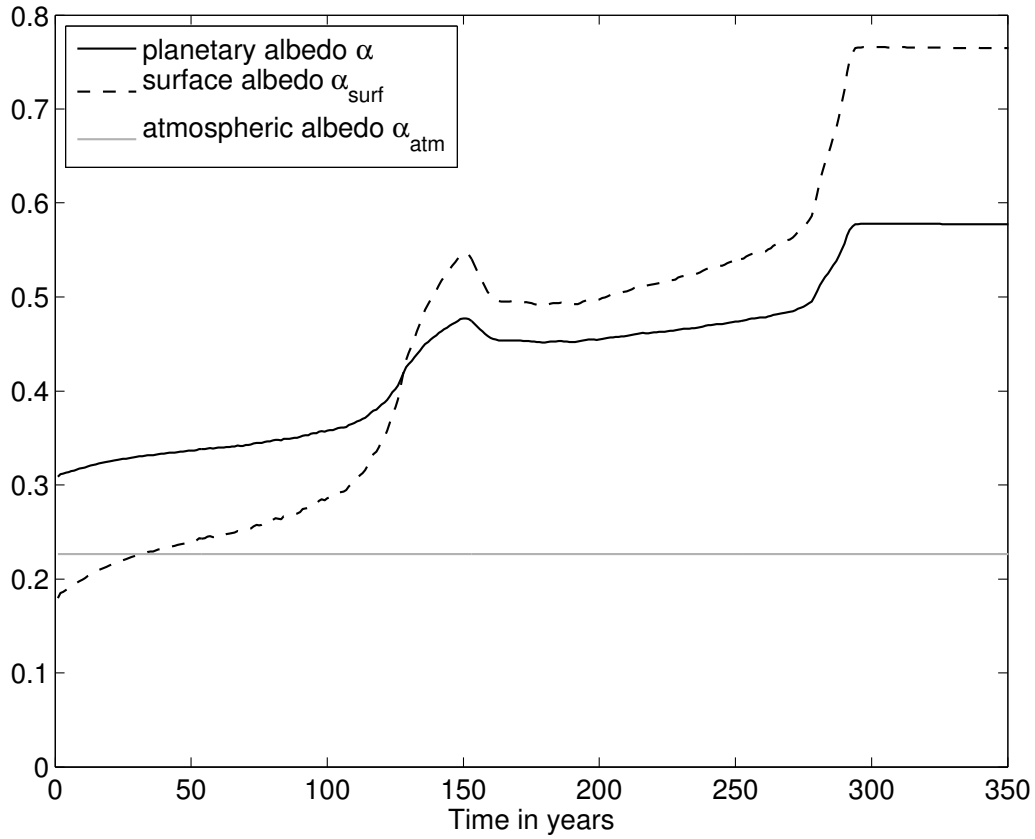

Figure 6: Annual globally averaged planetary (solid line), surface (dashed line) and atmospheric (grey line) albedos for the SC0.91noVegNPZD_const_CO2 model run.

Figure 7 shows the heat fluxes between the ocean and the atmosphere. Ocean heat fluxes of 13, 9 and 6 PW occur at the beginning of the model runs with a solar radiation reduced to 87%, 91% and 94%, respectively. The heat fluxes of the corresponding model

runs from Voigt and Marotzke (2009) results in higher values with 7.5, 5 and 3 PW, respectively. During phases of fast sea ice expansion both models show an enhanced ocean heat loss.

A detailed comparison of the simulation SC0.91noVegNPZD_const_CO2 to the corresponding simulation of Voigt and Marotzke (2009) can be found in the following. In the SC0.91noVegNPZD_const_CO2 simulation the heat flux decreases until year 120 from 9 to 4 PW, then during the first phase of sea ice expansion the heat flux increases up to 5 PW and afterwards it falls to 1.5 PW. During the second sea ice expansion phase a strong ocean heat loss of 1.8 PW is observed (phase 1: year 110 until year 150, phase 2: year 280 until year 293). In year 430 the heat flux decreases to nearly zero PW. In the corresponding model run from Voigt and Marotzke (2009) the heat flux decreases from from 5 PW below 2.5 PW after roughly 50 years, then it decreases further and stabilizes at around 1.5 PW. During the phase of fast sea ice expansion it shows an ocean heat loss peak of 5.5 PW. The amplitude of this peak is much higher than the peaks in the corresponding events in the UVic model run. However the UVic model shows stronger ocean heat fluxes at the beginning of the model run, where the ocean heat flux drops below 2.5 PW in year 150, which is 100 years later than in the ECHAM5/MPI-OM model.

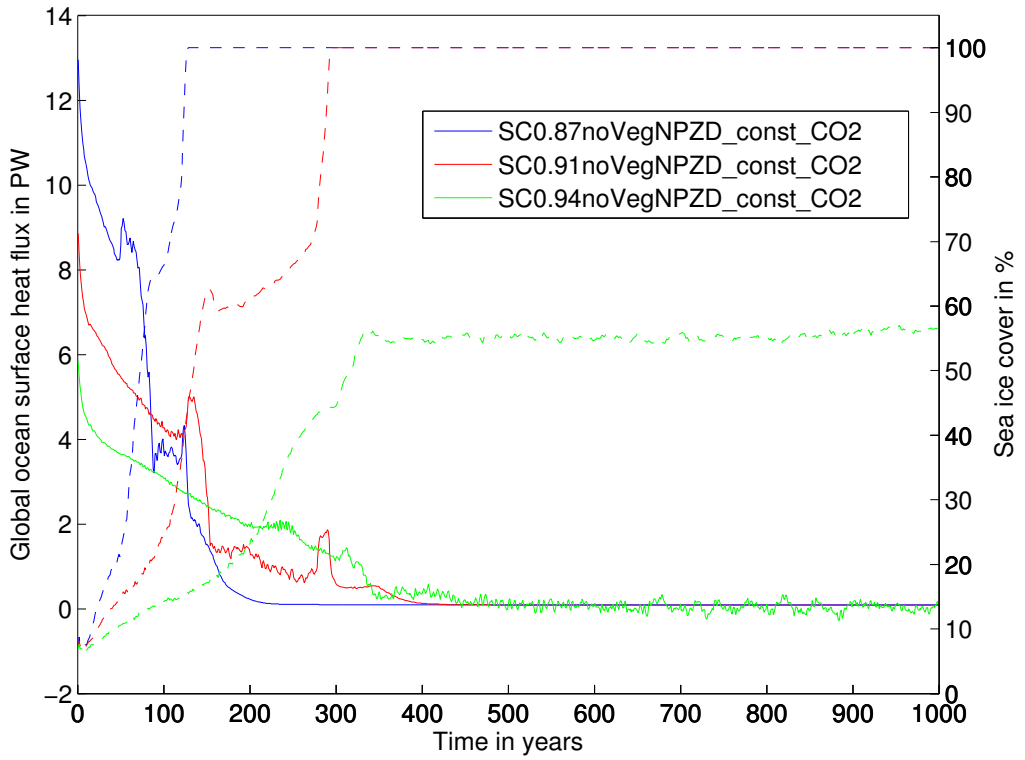

Figure 7: Upward global averaged ocean surface heat flux in PW (solid lines) and global averaged sea ice cover in percentage of the global ocean (dashed lines). Solar irradiance is set at the beginning at a fixed values of 87% (blue), 91% (red) and 94% (green).

3.2 Impact of the Carbon Cycle on the Development of a Snowball Earth

3.2.1 Sensitivity to Variation in the Solar Forcing

This chapter determines the influence of the land and ocean carbon cycle on the development of a Snowball Earth with a varying solar forcing. Therefore model runs are carried out with reduced incoming solar radiation ranging from 6 - 50% with and without the land and marine carbon cycle. At the end of this chapters a fixed reduction in incoming solar radiation was chosen for the following investigations.
Figure 8 shows the sea ice expansion and carbon dioxide concentrations for model runs without NPZD, without vegetation module and fixed carbon dioxide concentration (solid lines) and model runs with implemented NPZD, implemented vegetation module and variable carbon dioxide concentration (dashed lines). For different prescribed solar irradiance, the difference of both model run types represents the effect of the carbon cycle on the development of a Snowball Earth. In general the model runs with carbon cycle show a delay in reaching Snowball Earth.

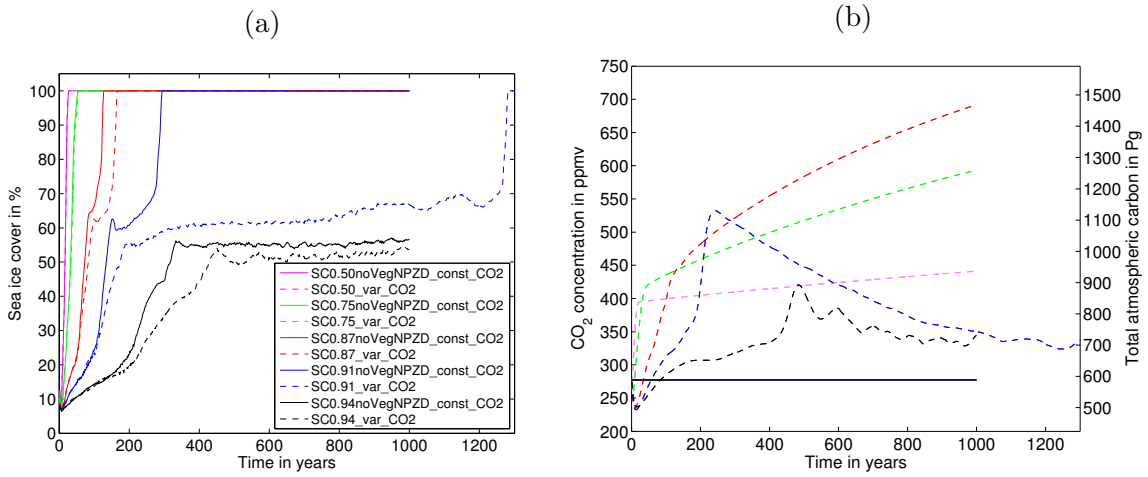

Figure 8: (a) Annual globally averaged sea ice cover and (b) the total atmospheric carbon dioxide concentration in ppmv and absolute carbon content in PgC. Solar irradiance is set at the beginning at fixed values ranging from 50% to 94%. Solid (dashed) lines denote model runs with constant (variable) carbon dioxide and without (with) Vegetation and NPZD model.

Due to a reduction in atmospheric carbon dioxide concentration, the sea ice expansion accelerates during the first approximately 20 years for models runs with variable carbon dioxide concentrations in comparison to the non carbon cycle simulations. This acceleration can increase the sea ice expansion by only 0.5% and is completely compensated after 20 to 100 years by increased carbon dioxide concentrations.

Ongoing increase in carbon dioxide concentrations further acts to stabilize and delay sea ice expansion due to an enhanced green house effect. For a strong reduction in incoming solar radiation to 50% and 75% of the preindustrial solar constant (PSC), carbon dioxide increases to 395 and 423 ppmv respectively, but shows nearly now influence on the sea ice expansion (magenta and green lines in figure 8a). The increase of carbon dioxide concentrations from preindustrial 280 ppmv to 395 and 423 ppmv corresponds to a greenhouse effect of 1.8W/m^2 and 2.2W/m^2, which seems to be negligible in comparison to the forcing due to the initial reduction in solar radiation. For 87% PSC the implementation of the carbon cycle delays Snowball Earth by 38 years, even though the carbon dioxide concentrations are lower for the first 100 years in comparison to the 50% and 75% PSC model runs.
In the 91% PSC model runs the carbon cycle delays the development of Snowball Earth by roughly 1000 years. In this simulation the climate shows largest sensitivity to changes in carbon dioxide concentration, therefore the subsequent chapters focus on the 91% PSC scenario. The carbon dioxide concentrations for the model run with carbon cycle ranges from 232 to 532 ppmv with a respective greenhouse forcing from -1 to 3.4 W/m^2. Snowball Earth is reached in year 1282 with a carbon dioxide concentration of 330 ppmv.

3.2.2 Snowball Earth without Carbon Cycle

The development of Snowball Earth in the model run with 91% PSC and without carbon cycle (SC0.91noVegNPZD_const_CO2) shows a continuous increase in sea ice cover for the first 150 years (figure 9d) and a shift of the sea ice edges (90% sea ice fraction) equatorward to 23°N and 5°S. Afterwards sea ice expansion is stopped in the southern hemisphere until year 260. In the northern hemisphere the sea ice edge is pushed back to 32°N and moves again southward until year 260. The second phase of fast sea ice expansion starts in year 280 and ends in year 277 with the whole ocean sea ice covered. Figure 9a shows the development of the sea surface temperature (SST) with black lines indicating the transition region from 90% to 10% zonal mean sea ice fraction. Temperature changes only occur in regions of open ocean, because in sea ice covered regions the temperature will be held to the freezing point. Maximum temperatures are centered around 10°N and decrease from 27 °C to 10 °C in year 140. Afterwards the ocean warms up to 20 °C in year 170. This warming event extends in meridional direction from the equator to 25°N and vanishes at the beginning of the second phase of fast sea ice expansion. The surface salinity (Figure 9b) shows a different pattern. Sea surface salinity does not stay constant under sea ice in contrast to the SST and controls the surface density (see Figure 9c), determining regions of subduction and convection. In polar regions the ocean salinity is generally increasing with time and after reaching Snowball Earth state everywhere. In the open ocean and especially in the sea ice transition regions the surface water is freshening. During the first phase of sea ice expansion (year 110 to 150) a salinity

minimum of 32.4 occurs in the southern transition region and during the warming event a large scale salinity minimum appears extending over the whole subtropics and tropics. This minimum vanishes as soon as Snowball Earth is reached.

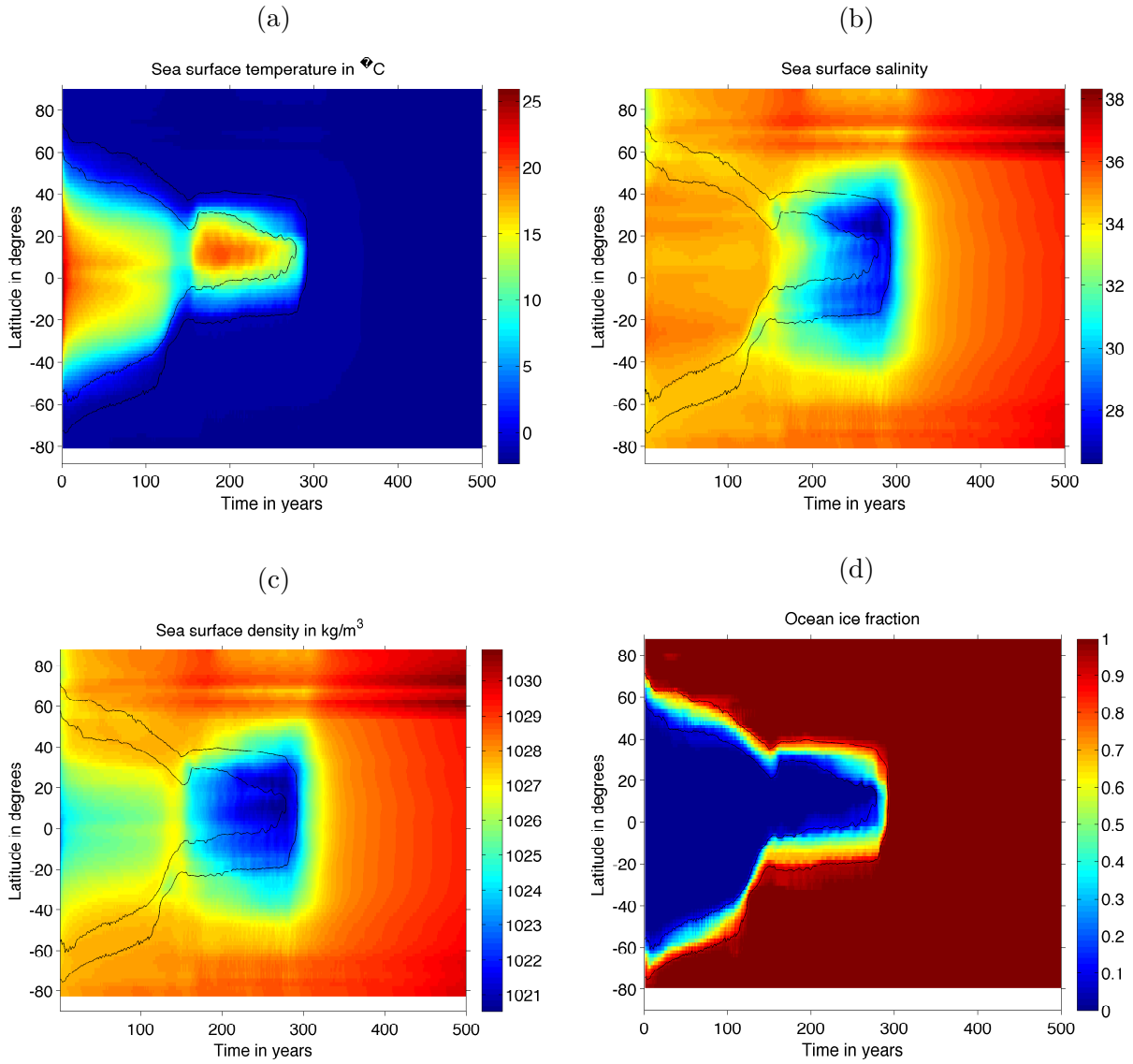

Figure 9: Hovmöller plots showing the annual zonal averages at the sea surface for (a) temperature, (b) salinity, (c) density and (d) ocean ice fraction. The inner (outer) black isoline indicates 10% (90%) ocean sea ice cover. Data from model run SC0.91noVegNPZD_const_CO2.

Salinity changes can appear due to oceanic advection and mixing processes or due to freshwater fluxes at the sea surface. The ocean volume in the UVic model is held constant so a upward freshwater flux is modeled by a virtual downward salinity flux defined by

$$Q_S = \rho_0 \cdot S^*(E - P - R - L) \tag{8}$$

with $S^* = 34.9$ the representative salinity for the ocean, E the evaporation, P the precipitation of water, R the runoff from land and L the salt flux due to freezing ocean water and melting sea ice. Figure 10a shows the virtual salinity flux with a strong freshening signal in the sea ice transition region and with a positive salt flux in sea ice covered regions caused by salt brine release due to the freezing of sea ice as well as a freshening of the transition regions at sea ice edges. This effect is strongest at the southern edge from year 150 to year 270.

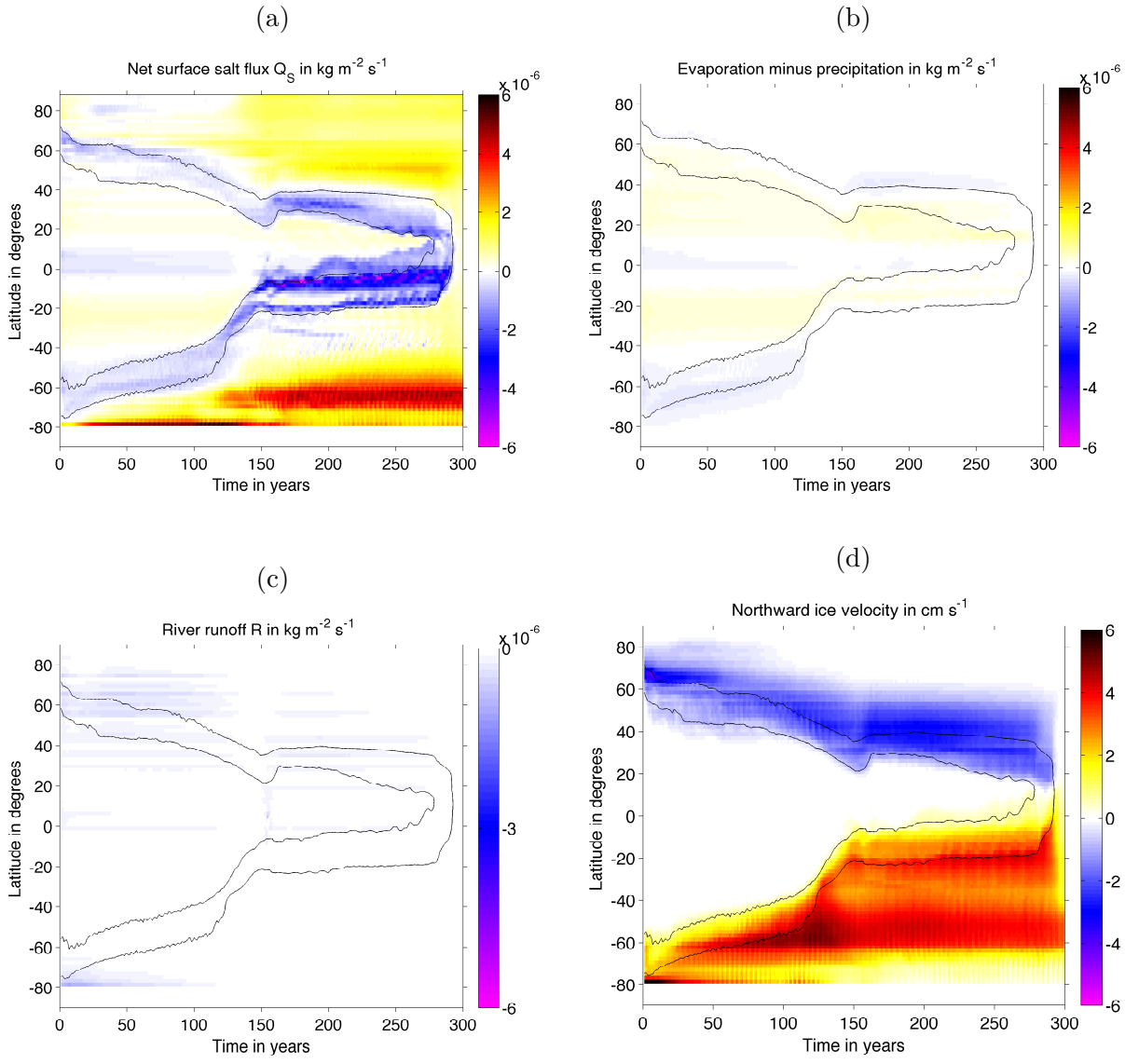

Figure 10: Hovmöller plots showing the annual zonal averages at the sea surface for (a) virtual salinity flux, (b) evaporation minus precipitation (as salt equivalent) and (c) the river runoff (as salt equivalent); (d) shows the northward ice velocity. The inner (outer) black isoline indicates 10% (90%) sea ice cover. Data from model run SC0.91noVegNPZD_const_CO2.

In the zonal mean the sea ice velocities are directed equatorward with the speed ranging from 2 to 6 cm/s (see figure 10d). During the above mentioned large scale freshening event the sea ice edge remains nearly at the same latitude, so that the sea ice at the sea ice edges has to be melted.
The net effect of evaporation and precipitation (Figure 10b in salt equivalents) shows a freshening near the equator and a positive net effect in the off equatorial open ocean regions and in the sea ice transition regions. However this net effect as well as the effect of the river runoff (see figure 10c) on the salt flux are negligible in comparison to the freshening due to the melting of sea ice.
It is not possible to calculate the freshwater fluxes L into the ocean due to melting and freezing of sea ice as a residual from equation (8), because the model outputs evaporation and precipitation does not only include freshwater fluxes between the atmosphere and ocean and land surfaces, but also includes freshwater fluxes between sea ice and atmosphere due to sublimation. Therefore the model outputs for evaporation and precipitation are not equal to those in equation (8).
In figure 9b a freshening also occurs in the open ocean. This freshening can only be due to the advection of melted water from the sea ice edges. The freshwater is transported equatorward and also under the sea ice which can be seen in figure 11b as the freshwater layer extending from 60°S to 60°N. The ice formation regions at the poles are characterized by deep water formation with a strong salt flux into the ocean due to brine formation. The signal of this high saline water can be followed down into the deep ocean and equatorwards.

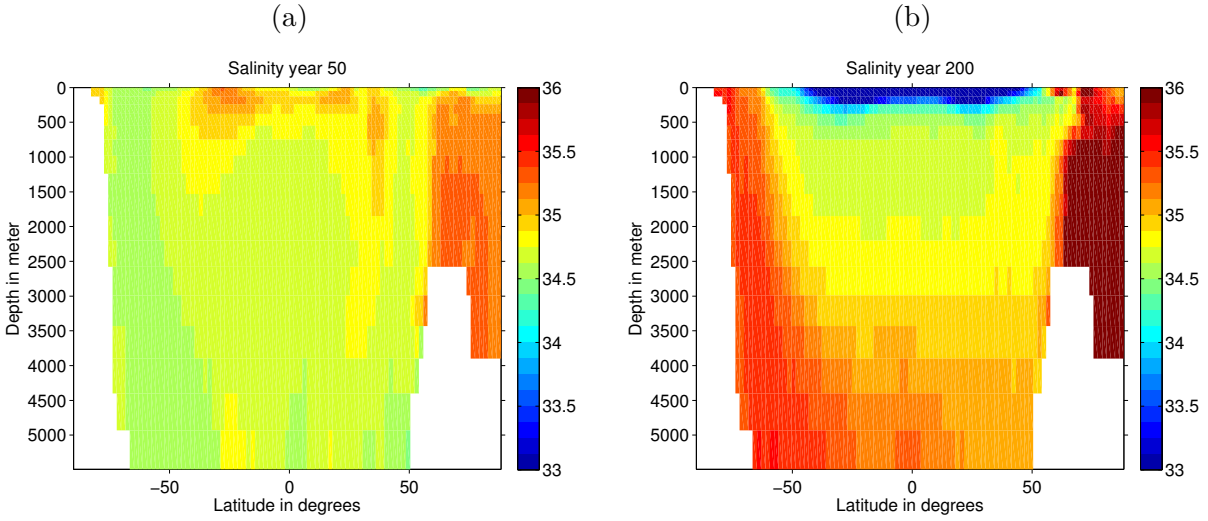

Figure 11: (a) Zonal averaged salinity in simulation year 50 (a) and 200 (b). Data from model run SC0.91noVegNPZD_const_CO2.

Although the sea ice formation is stronger in the southern hemisphere than in the northern hemisphere (see figure 10a) , the salinity is higher in the northern hemisphere,

concluding that the water masses can better expand from the southern ocean into the different ocean basins. In the northern hemisphere the deep water formation seems to be blocked and the salt accumulates north of 60°N. Figure 12 shows the salinity fluxes at the sea surface for year 150. A strong freshening signal can be seen at the ice edges (especially at the southern ones) and a large region of brine formation can be seen near Antarctica. There are a few places of enhanced sea ice formation in the northern hemisphere: In the western Labrador Sea, around the Grand Banks of Newfoundland, in the Bering Strait and in the Okhotsk Sea.

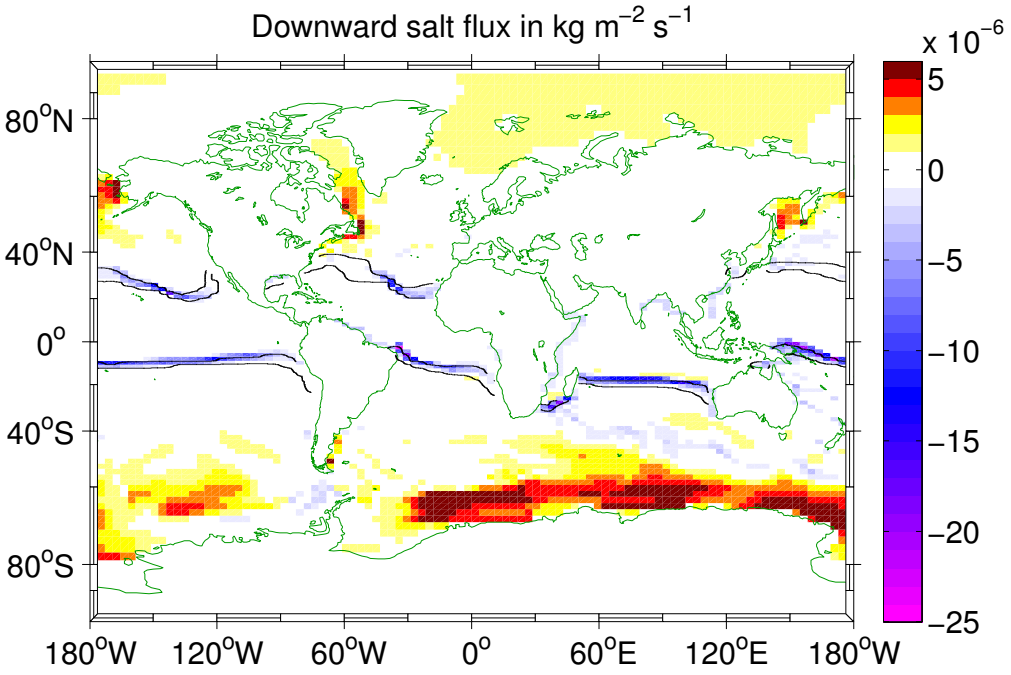

Figure 12: Annual globally averaged virtual salinity flux for year 150.The inner (outer) black isoline indicates 10% (90%) ocean sea ice cover. Data from model run SC0.91noVegNPZD_const_CO2.

The redistribution of the freshwater in the ocean from the poles equatorward shows also an influence on the subtropical cells (STCs). The STCs are responsible to transport heat from the equator into the subtropics and bring cold water back at shallower depths. The heat transport of the STC is influenced by the temperature field and by the volume transport. To analyze the volume transport the meridional overturning circulation (MOC) is determined by

$$\Psi_{ocean}(z,\varphi) = a \cdot \cos\varphi \int_{z}^{top} \oint_{\lambda} v d\lambda dz' \tag{9}$$

with a being the earth radius, φ the latitude and λ the zonal coordinate. The MOC for the reference run is shown in figure 13e representing in the following the structure

of the STC with 70 SV upwelling in the equatorial region and a meridional extend from 25°S to 25°N, reaching a depth of 200 to 250 m. The Snowball Earth simulation shows another STC structure. In year 150 (figure 13c) parts of the STC reaches very deep and the southern STC core is concentrated near the equator with the downward branch near the sea ice edge. From year 150 to 200 the freshening of the surface water increases the vertical density gradient and inhibit the deep water formation. The equatorial upwelling due to the STC weakens from 80 to 50 Sv by nearly 40%.

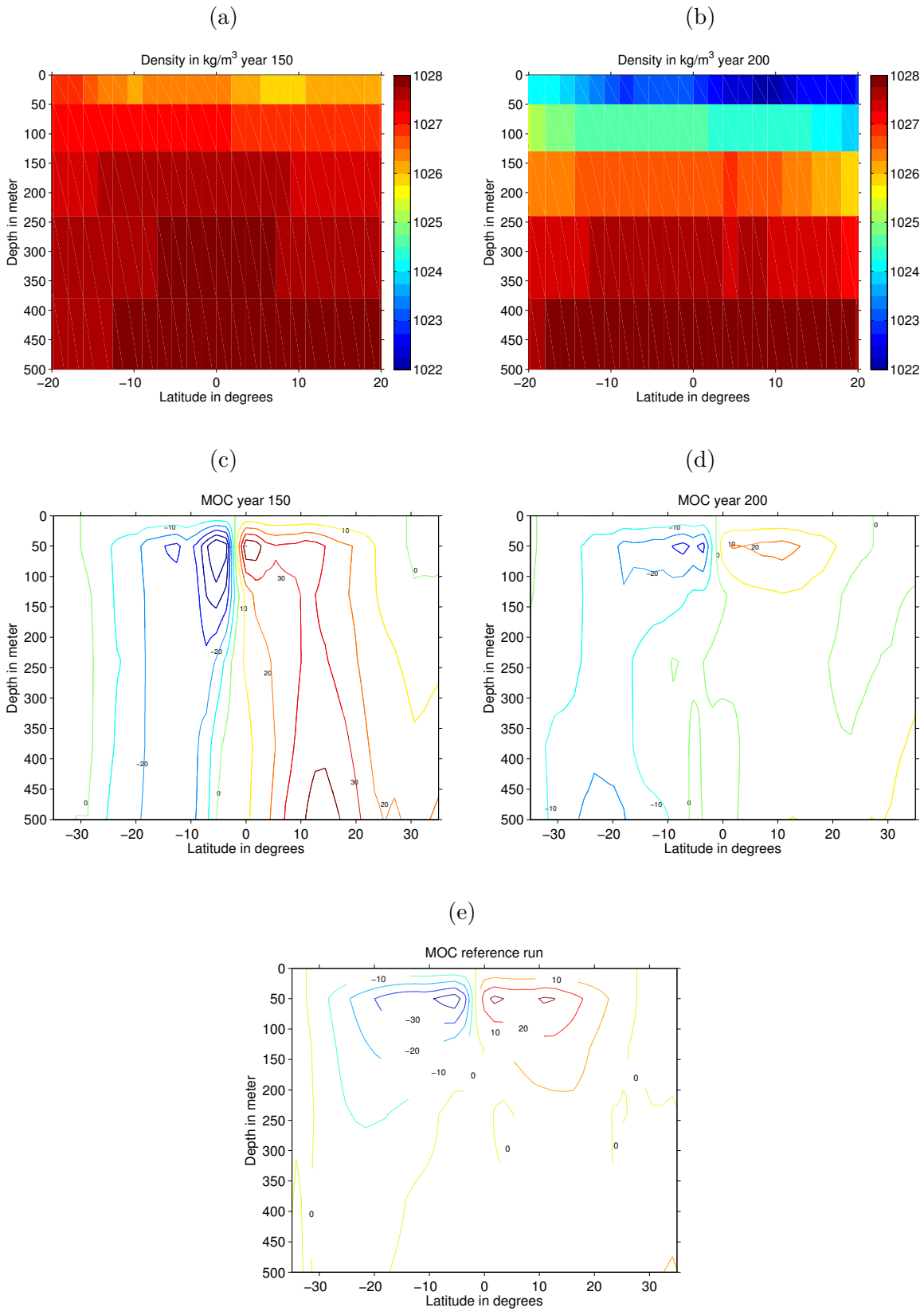

Figure 13: Annual zonally averaged vertical structure of potential density calculated from salinity and potential temperature for year 150 (a) and 200 (b). Meridional Overturning Circulation Ψ_{ocean} for year 150 (c), 200 (d) and for the reference run (e) in Sv. Data from model run SC0.91noVegNPZD_const_CO2 (a) - (d); SC1.0noVegNPZD (e).

But the above mentioned decrease in the MOC does not cause a decrease in the meridional heat transport of the same magnitude defined as

$$H_{ocean}(\varphi) = \rho_0 c_w a \cos\varphi \oint_{\lambda} \int_{bottom}^{top} vT dz d\lambda \tag{10}$$

with c_w=4.18·10$^3 Jkg^{-1}K^{-1}$ being the specific heat of water and with ρ_0=1027 kg m^{-3} being the reference density of sea water. Figure 14a shows the meridional heat transport. The maximum meridional difference of the meridional heat transport is 3.6 PW in year 150 and 3.5 PW in year 200 and peaks with 4.3 PW in year 160. The increase in sea surface temperature in equatorial regions is responsible for this peak in the meridional heat transport. Stronger meridional temperature gradients are compensating the weakening of the tropical MOC.

The cooling of the equatorial ocean enhances due to melting sea ice during the warm phase. Figure 14b shows the meridional latent heat transport due to sea ice calculated with the meridional transported sea ice volume and with the melting enthalpy of sea ice of 305 ·10$^6 Jm^{-3}$. The meridional heat transport increases from nearly 0 PW in year 100 to 2 PW in year 270 in the south and from 0 to -0.5 PW in year 279 in the north.

Very interesting is also the behavior of the meridional heat transport during the first 150 years. In year 76 the maximum meridional difference of the meridional heat transport reaches its maximum with a poleward heat transport of 5.4 PW and from there it decreases to the above mentioned 3.6 PW in year 150.

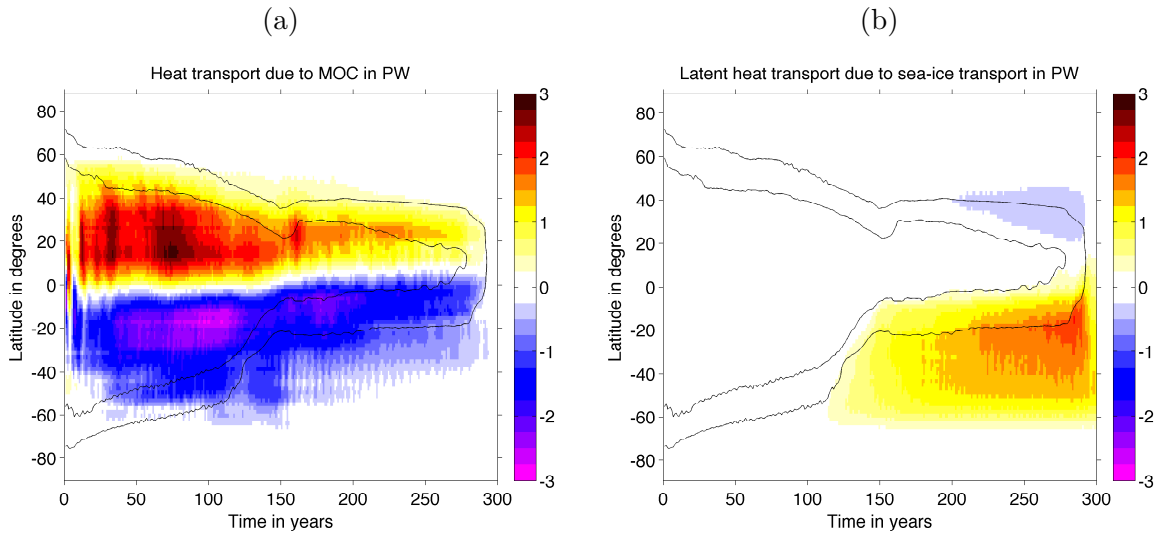

Figure 14: Meridional heat transport due to (a) the oceanic meridional overturning circulation (MOC) and due to (b) the latent heat transport of sea ice as annual values and zonally averaged. The inner (outer) black isoline indicates 10% (90%) ocean sea ice cover. Data from model run SC0.91noVegNPZD_const_CO2.

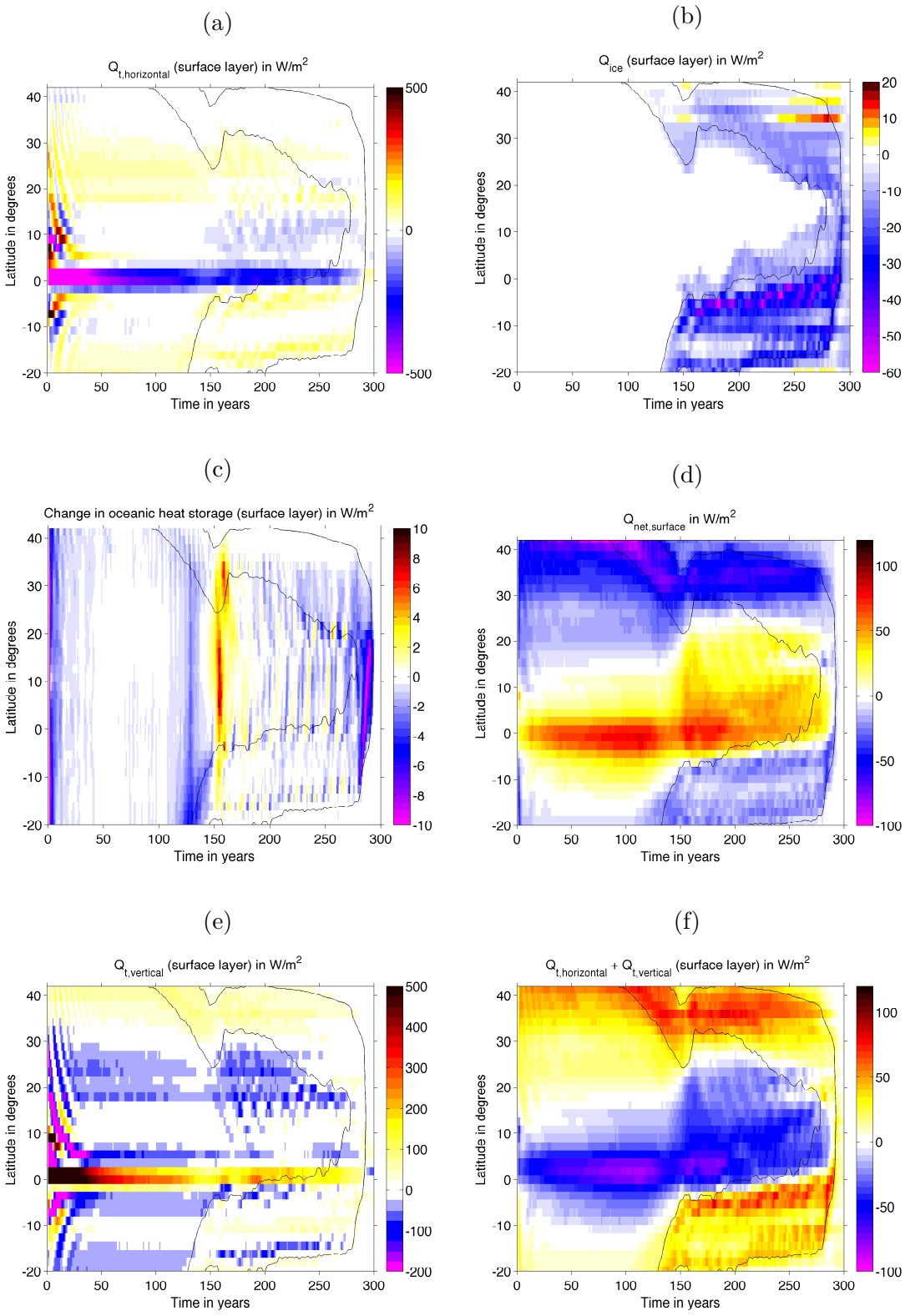

Figure 15: Hovmöller plots with annual zonal averages for (a) convergence of the horizontal heat transport $Q_{T,horizontal}$ (equation (10); (b) latent heat flux due to sea ice melting; (c) change in heat storage; (d) sea/ice surface net downward heat flux; (e) vertical oceanic heat transport $Q_{T,vertical}$ from below (as residual from equation (11)); (f) net heat transport $Q_{T,vertical} + Q_{T,horizontal}$. Positive values indicates heat flux into the ocean surface layer. Data from model run SC0.91noVegNPZD_const_CO2.

In the following the heat fluxes of the surface ocean layer are investigated between 40°N and 20°S to give a complete overview over all involved processes and to show the influence of the above mentioned freshening and warming of the open ocean. The convergence of the meridional heat transport $Q_{t,horizontal}$ (Figure 15a) and the convergence of the latent heat transport due to sea ice Q_{ice} (Figure 15b) are computed to get a corresponding heat flux in W/m². Then the vertical heat flux $Q_{t,vertical}$ (Figure 15e) into the surface layer is computed as an residual from the energy balance equation given as

$$\rho_{ref} c_w h \frac{\partial T}{\partial t} = Q_{t,horizontal} + Q_{t,vertical} + Q_{ice} + Q_{net,surface} \tag{11}$$

with h = 50 m being the thickness of the surface layer and $Q_{net,surface}$ (Figure 15d) including the latent heat flux due to evaporation and sublimation, the sensible heat flux and the heat flux due to long- and shortwave radiation. The left side of the equation gives the change in surface layer heat storage (figure 15c) derived from the changing ocean temperature in the surface layer. To analyze the net effect of the heat advection, the horizontal plus vertical heat fluxes are plotted in figure 15f.

At the beginning of the simulation the ocean is strongly cooled followed by a moderate cooling until in year 120, again followed by a stron cooling until year 140. From year 150 to year 160 a warming signal appears with a maximum of 7.6 W/m² at 11.7°N in year 154. This has to be caused by the increase of the heat flux $Q_{net,surface}$, because the heat flux due to advection (Q_t) decreases at the same time. This decrease of Q_t is driven by the increase in the meridional temperature gradient (see figure 16). This is in contrast to the first 130 years, here the increase in the the meridonal heat transport is driven by a stronger STC.

The latent heat flux due to ice melting shows strong heat fluxes up to 60 W/m² and plays an important role for the equatorward heat transport in the southern hemisphere.

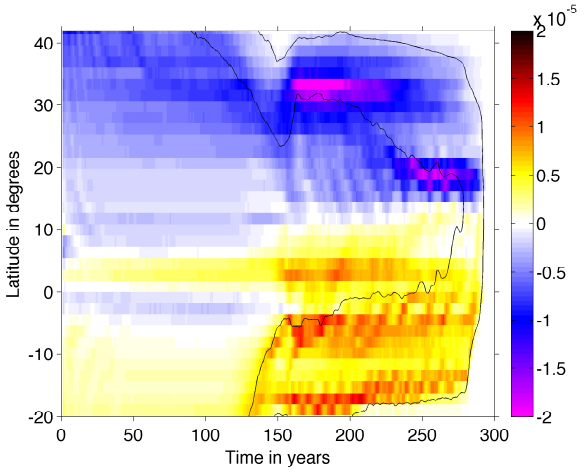

Figure 16: Meridional sea surface temperature gradient in °C/m. Data from model run SC0.91noVegNPZD_const_CO2.

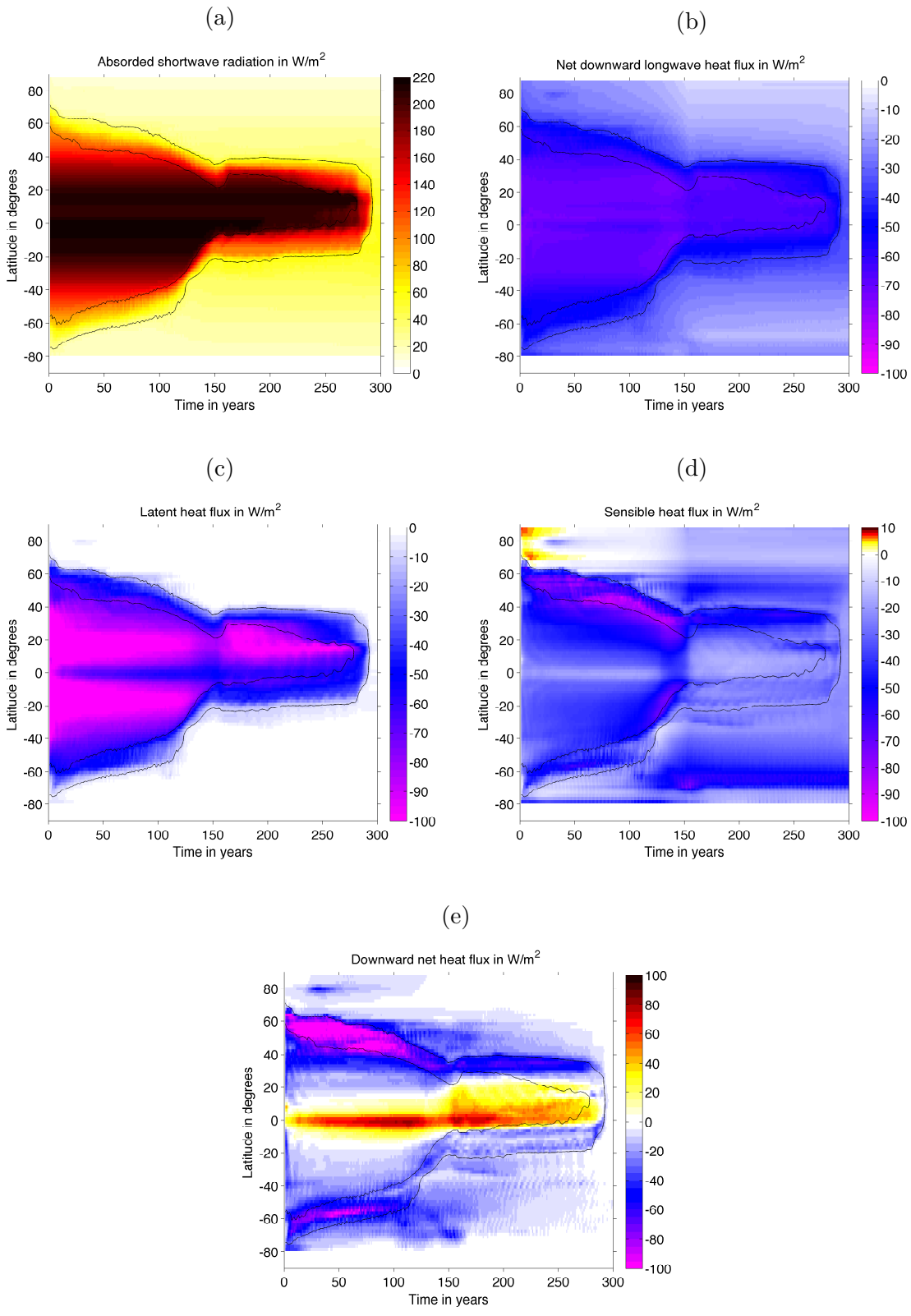

Figure 17: Hovmöller plots showing the annual zonal averages of the heat fluxes at the atmospheric/ocean boundary layer for (a) absorbed shortwave radiation; (b) net longwave radiation; (c) latent heat flux due to evaporation and sublimation; (d) downward sensible heat flux; (e) net downward heat flux. Positive values denote heat flux into the ocean surface layer. The inner (outer) black isoline indicates 10% (90%) sea ice cover. Data from model run SC0.91noVegNPZD_const_CO2.

Figure 17 (a)-(d) shows the different components of $Q_{net,surface}$. The net heat flux shows strong cooling at the ice edges mainly due to the sensible heat flux with the exception of the southern sea ice edge from year 150 to 300 where sea ice melting is the dominant forcing, as mentioned before. The net heat flux shows also strong warming in the equatorial region due to incoming shortwave radiation.

To come back to the initial question, what drives the warm phase, it is very interesting to see that the increase in the sensible heat flux is at the same time as the warming phase appears. Figure 18 shows the change (since year 140) of heat fluxes into the oceanic surface layer averaged over the northern tropical ocean. The change in the sensible heat flux (solid red line) explains most of the change in the net surface heat flux (solid green line). However, the increase in the net downward long wave radiation also plays an important role (blue line). With increasing sea surface temperature one would expect an increase in the outgoing longwave radiation called the Stefan Boltzmann Feedback, but in this case the increase in water vapor in the atmosphere (not shown) causes a strengthening of the clear-sky green house effect by acting as a positive feedback. This water vapor feedback dominates the change in net incoming long wave radiation during the warm event.

A large amount of the heat is transported away from the surface and into deeper layers by mixing or in the horizontal direction by advection (green dashed line) and also by the reduction of the incoming shortwave radiation (solid black line) due to the increase in sea ice cover. In the following I want to focus on the reaction to the ocean on the changes in sea ice cover and the warming event.

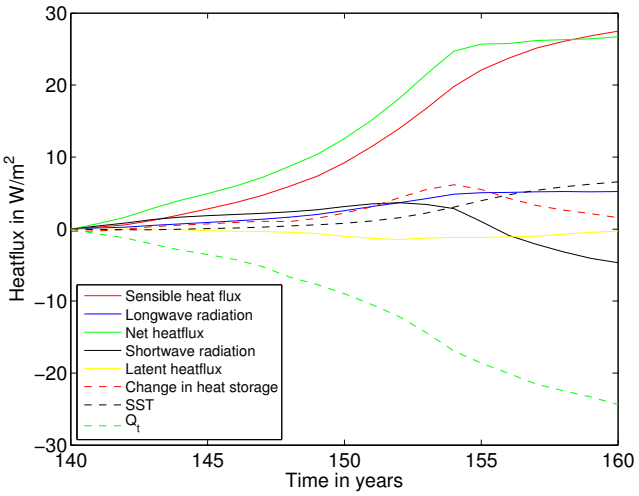

Figure 18: Solid lines denote the change in annual mean heat fluxes at the boundary layer between ocean/ice and atmosphere for the northern tropical region (EQ - 23°N); change in heat storage (dashed red line, absolute values), sea surface temperature anomaly (dashed black line in °C) and the convergence of oceanic heat transport (dashed green line) of the ocean surface layer (50m) for the northern tropical region. Positive values denote the heat flux anomaly into the ocean surface layer relative to year 140 (with the exception of the change in heat storage).model run: SC0.91noVegNPZD_const_CO2

The change in oceanic heat transport is shown again in figure 19 with both components for the change in the vertical oceanic heat transport (dashed black line) and the change in horizontal oceanic heat transport (dashed blue line). The meridional poleward heat transport increases as the sea surface temperature and (solid black line) the meridional temperature gradient (shown in figure 16) increase. The vertical heat transport initially drops until year 155 on -12 W/m^2, but then rises back to -7W/m^2 and remains there. The vertical heat transport is representative for the effect of convection, mixing and upwelling which partially depends on the density stratification.

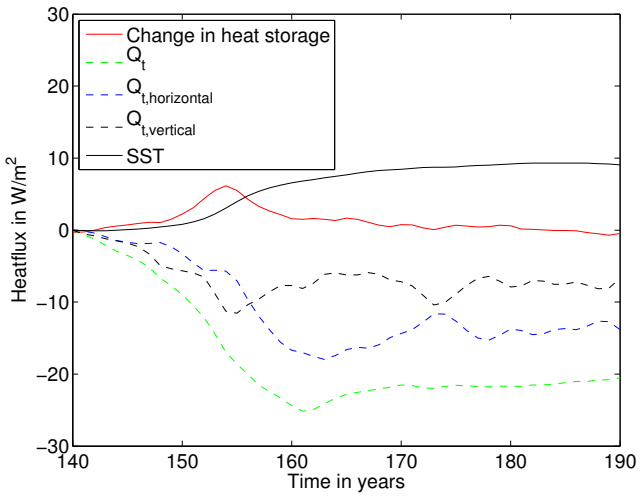

Figure 19: Anomaly of the annual mean oceanic heat transport (solid green line) averaged over the northern tropical region (EQ - 23°N) relative to year 140 with the vertical component (dashed black line) and the horizontal component (dashed blue line) also shown. Positive values denote heat flux anomalies into the ocean surface layer. The change in heat storage is given as absolute values (dashed red line). Sea surface temperature (SST) anomaly in °C (dashed black line). model run: SC0.91noVegNPZD_const_CO2

The density difference between the upper two ocean layers (solid green line figure 20a) represents the stratification of the surface ocean. Stratification increases strongly from 0.6 kg/m^3 in year 150 to 1.5 kg/m^3 in year 163. The meridional advection of low salinity water and the warming of the surface water are the main driver of the change in density structure. To differ between these two processes the effect of salinity and temperature on the stratification are shown in figure 20b. To calculate the effect of salinity/temperature on stratification, density was calculated with a reference temperature/salinity field of year 140. Note that the non-linearity of the equation of state causes errors for the averaged value of less than 0.002 kg/m^3. Freshening due to melting sea ice plays a major role in the changes in stratification and with this also in the shallowing of the meridional overturning circulation and the cut off from the deep water branches (see figure 13c, 13d).

In the following the atmospheric components of the warming phase are investigated to find out what the initial driver is for the change in sensible heat flux. The sensible heat flux is calculated in the UVic model with a bulk parametrization

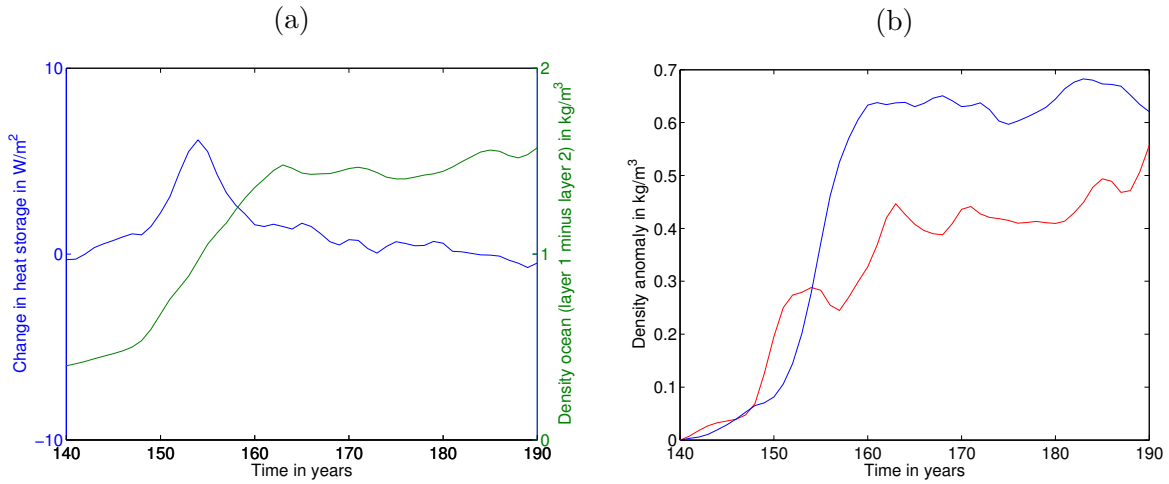

Figure 20: (a) Annual average density difference between the upper two ocean layers (dashed green line) and the annual average change in ocean heat storage averaged over the northern tropical region (EQ - 23°N); (b) Effects of salinity (solid blue line) and temperature (solid red line) on the density difference shown in (a). Data from model run SC0.91noVegNPZD_const_CO2.

$$Q_{SH} = \rho_a C_H c_{pa} U (T_A - T_S) \tag{12}$$

where $C_H = 0.94 C_E$, U is the surface wind speed and $T_A - T_S$ is the temperature difference at the atmosphere-ocean boundary. $C_E = 1.4 \cdot 10^{-3}$ is the dalton number and is not time-dependent. Therefore the change in the sensible heat flux mainly depends on the temperature difference at the atmosphere-ocean interface as shown in figure 21. Figure 21b shows the convergence of the horizontal heat transport of the atmosphere calculated as a residual from equation (2). The flux is averaged zonally over the land and ocean, representing the meridional advection of heat due to atmospheric transport. During the first 120 years heat is transported from the sub tropics poleward, cooling the open ocean regions and warming the sea ice covered regions. Around year 120 the strength of the poleward heat transport globally decreases.

In the northern tropical region the convergence of atmospheric heat reduces from -45 W/m^2 in year 120 to -7 W/m^2 in year 160 (figure 22a, blue line). This change in the atmospheric heat transport leads to a change in the sensible heat flux (figure 22a, red line) in slightly more than 10 years. So the atmospheric sensible heat flux, which is responsible for the warm phase, is driven by changes in atmospheric heat transport. Less heat is transported poleward and the atmosphere warms up, thus reducing the temperature difference at the boundary layer and with this the sensible heat flux.

The atmospheric heat transport depends mainly on the meridional temperature gradient and on the prescribed wind field. Figure 22b shows the surface air temperature and an

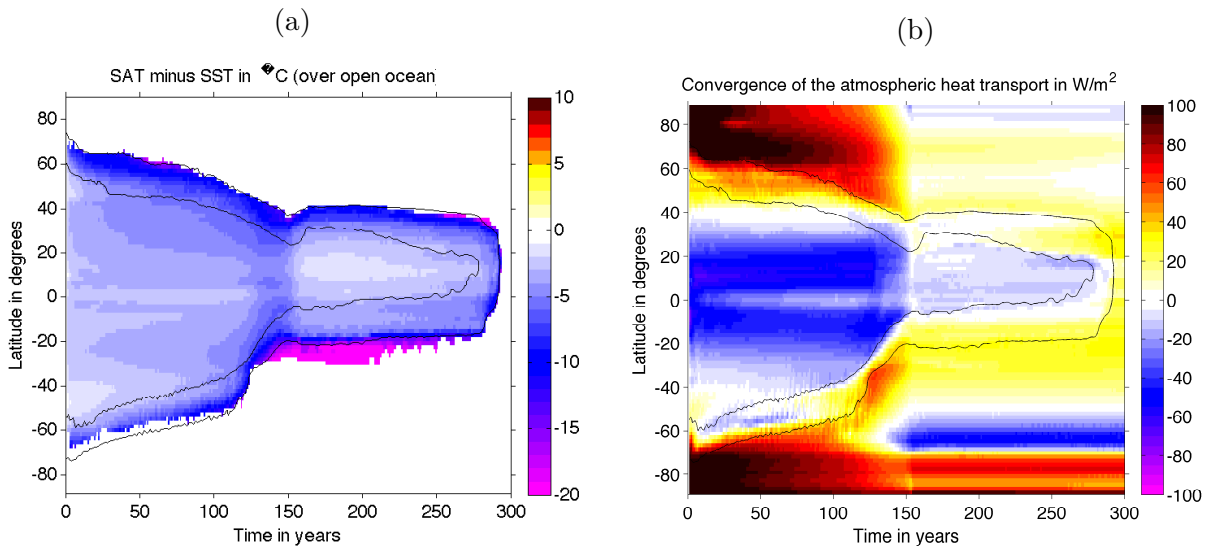

Figure 21: Hovmöller plots showing annual zonal averages of (a) surface air temperature minus sea surface temperature (only open ocean grid points) and (b) the convergence of the atmospheric heat transport Q_t, positive values denotes a heat flux into the atmosphere. Data from model run SC0.91noVegNPZD_const_CO2.

increase in the meridional gradient which is in contradiction with the previous findings. Experiments investigations a changing wind field and their effect on the development of a Snowball Earth and the development of the warm phase can be found in chapter 3.2.6.

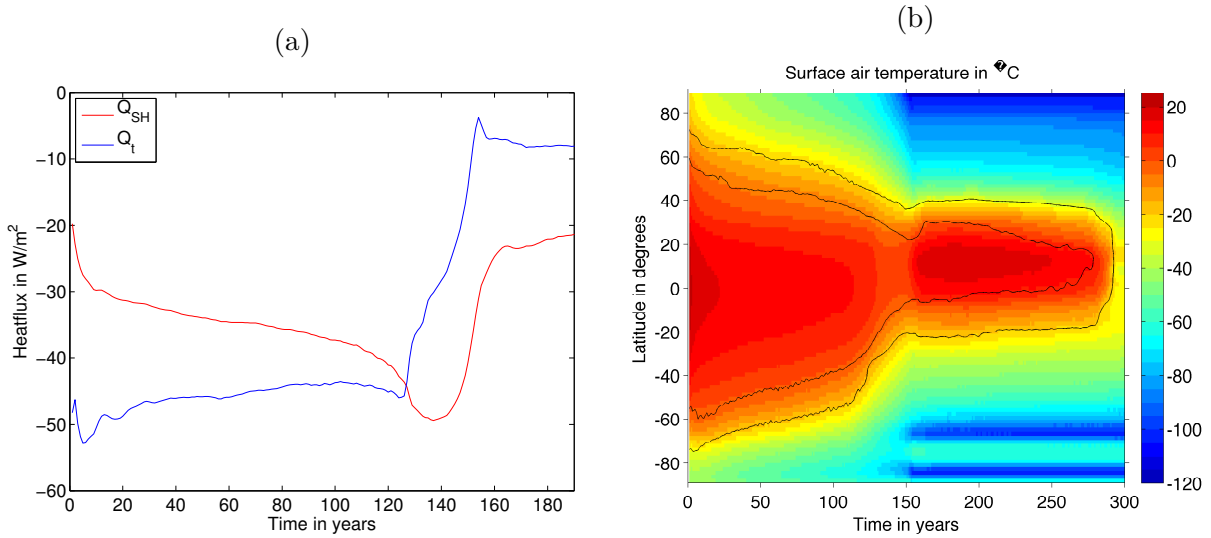

Figure 22: (a) Convergence of the annual mean atmospheric heat transport (blue line) and the sensible heat flux (negative values indicating a flux into the atmosphere) (red line) averaged over the northern tropical region (EQ - 23°N). (b) Hovmöller Plot with annual zonal averages of the surface air temperature. Data from model run SC0.91noVegNPZD_const_CO2.

3.2.3 The Solubility Pump

This chapter discusses the model run (SC0.91noVegNPZD_var_CO2) where atmospheric carbon dioxide concentrations change due to carbon dioxide fluxes between the ocean and the atmosphere. In general the cooler ocean surface temperature (in comparison to the preindustrial ocean) increase the solubility of carbon dioxide. Thus enhances the ocean uptake of carbon dioxide (see figure 23a), especially during the first 50 years of the simulation. Then the reduction in the flux that occurs is caused on the one hand by the smaller changes in the sea surface temperature and on the other hand by the expansion of sea ice, which inhibits gas exchange between the ocean and the atmosphere. This simulation much like the SC0.91noVegNPZD_const_CO2 model run with a warm phase appearing around year 150. During the warm phase carbon dioxide is outgassing, but also a large amount of carbon dioxide is exported as falling detritus in the deep ocean. These high carbon dioxide waters are trapped in the deep ocean due to stratified equatorial surface waters.

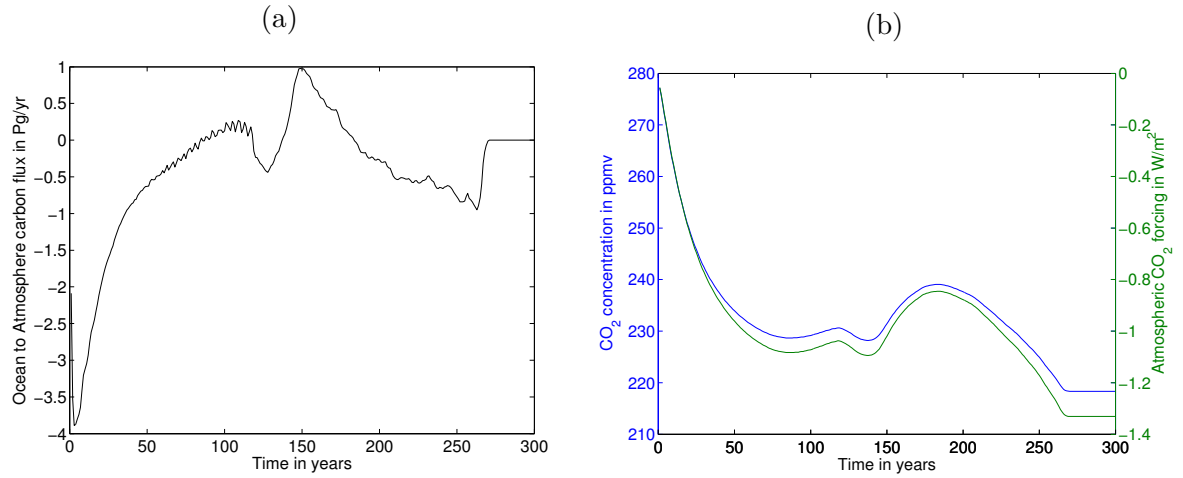

Figure 23: (a) Annual globally averaged ocean to atmosphere carbon CO_2 flux and (b) the total atmospheric carbon concentration (blue). The corresponding atmospheric forcing due to CO_2 for air temperatures above 220 K is also depicted. Data from model run SC0.91noVegNPZD_var_CO2.

The atmospheric carbon dioxide concentration is shown in figure 23b along with the influence of the carbon dioxide concentration on the clear-sky greenhouse effect G (see equation (5), p.10), e.g., the atmospheric carbon dioxide forcing. The reduction in carbon dioxide reduces the atmosphere forcing by a maximum of 1.4 W/m^2.
The differences in sea surface temperature, salinity, density and ocean ice fraction from the reference run (SC0.91noVegNPZD_const_CO2) are shown in figure 24. The weaker greenhouse effect causes a 24 year earlier development of a Snowball Earth, e.g. in year 271, (see figure 24d) with a carbon dioxide concentration of 218 ppmv. The warm phase

also begins about 20 years earlier than in the reference run (see figure 24a). This also causes the earlier start of the freshening of the tropical ocean (see figure 24b).

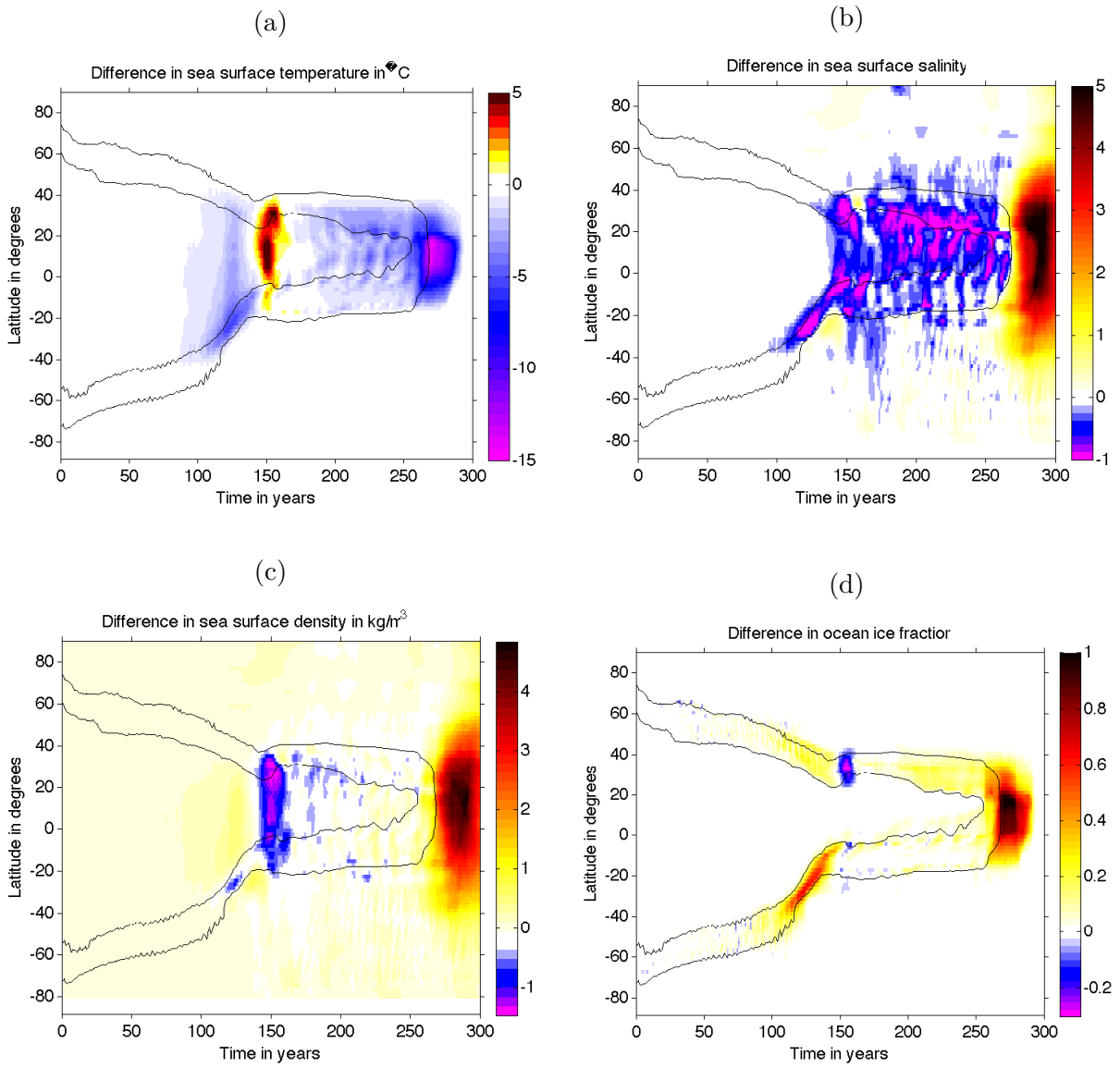

Figure 24: Hovmöller plots showing the annual zonal averages at the sea surface for (a) temperature, (b) salinity, (c) density and (d) ocean ice fraction calculated as anomalies (SC0.91noVegNPZD_var_CO2 minus SC0.91noVegNPZD_const_CO2). The inner (outer) black isoline indicates 10% (90%) sea ice cover for the model run SC0.91noVegNPZD_var_CO2.

Due to changes in the atmospheric carbon dioxide concentration the absorption potential for long wave radiation is reduced in the atmosphere and more radiation can be directly emitted to space, causing net heat loss, thus reducing the atmospheric temperature and driving a stronger sensible heat fluxe to the atmosphere (see figure 25b). These are the main drivers of the changing surface net heat flux over the ocean until the warm

phase begins (compare with figure 25a). These fluxes are also responsible for the generally higher sea surface density. After the warm phase other factors play an additional role in changing the surface net heat fluxes. However, these factors were not investigated in this study.

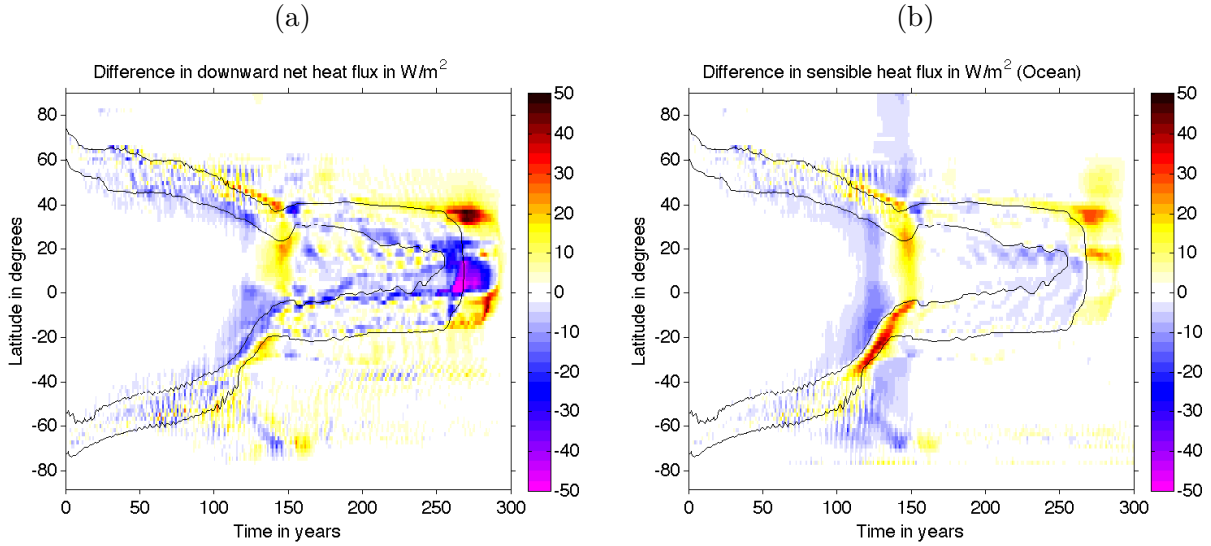

Figure 25: Hovmöller plots showing annual zonal averages of the heat flux anomalies at the ocean-atmosphere for (a) the net downward heat flux and (b) the downward sensible heat flux. Positive values denote a heat flux into the ocean. The inner (outer) black isolines indicate 10% (90%) sea ice cover.
(SC0.91noVegNPZD_var_CO2 minus SC0.91noVegNPZD_const_CO2)

The higher sea surface density acts to decrease the vertical density gradient and the potential for convection. This is important because convection is an important driver for the meridional overturning circulation and meridional heat transport. Thus, meridional heat transport (shown in figure 26b) is enhanced at the beginning of the simulation and continues to play an important role for the preconditioning of the ocean for the final freezing process in equatorial regions. During and after the warm phase the meridional heat transport decreases and the northward transport of latent heat due to sea ice increases, similar to the reference run. But for the SC0.91noVegNPZD_var_CO2 model run these processes occur earlier.

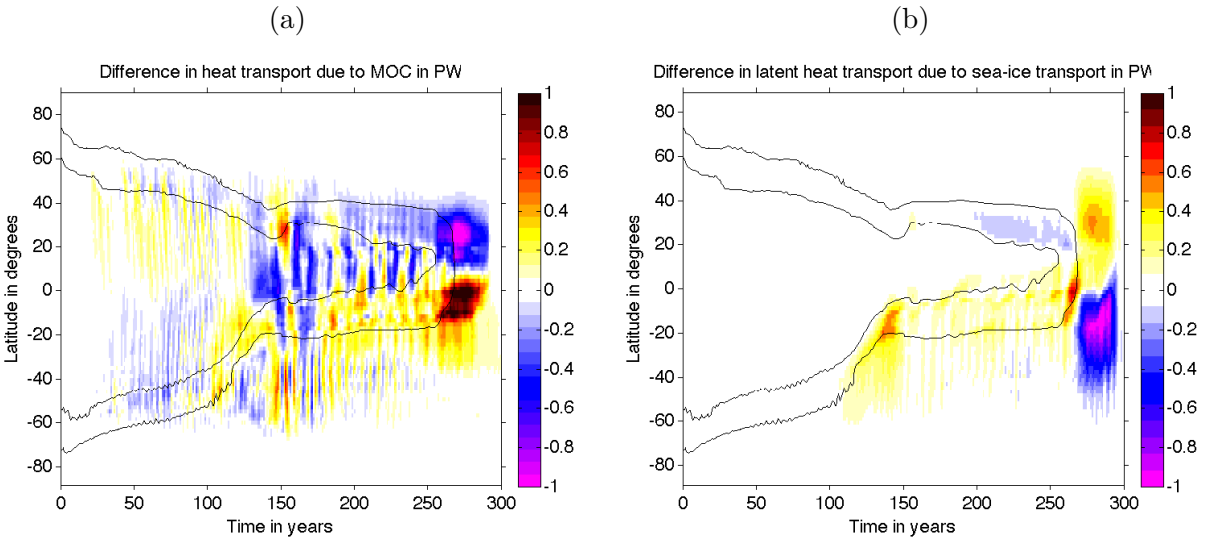

Figure 26: Hovmöller plots showing the anomalies of the meridional heat transport due to (a) the oceanic meridional overturning circulation (MOC) and due to (b) the latent heat transport of sea ice as a zonal average (SC0.91noVegNPZD_const_CO2 minus SC0.91noVegNPZD_const_CO2). The inner (outer) black isoline indicates 10% (90%) sea ice cover.

3.2.4 The Marine Ecosystem

The marine ecosystem is represented in the UVic model by the Nutrient Phytoplankton Zooplankton Detritus (NPZD) model and it is activated in the SC0.91noVeg_var_CO model run in order to analyse the influence of the marine ecosystem on the development of a Snowball earth. The marine ecosystem can influence the atmospheric carbon dioxide concentration and hence the green house effect in the UVic model. The ocean outgases 150 Pg carbon during the first 100 years and takes additional 150 years to store this excess of carbon back in the ocean (see figure 27b). This carbon dioxide anomaly in the atmosphere delays Snowball Earth for 36 years in comparison to the SC0.91noVegNPZD_var_CO model run and 12 years in comparison to the SC0.91noVegNPZD_const_CO model run (see figure 27a). The carbon dioxide concentration drops to 251 ppmv until full sea ice cover is reached.

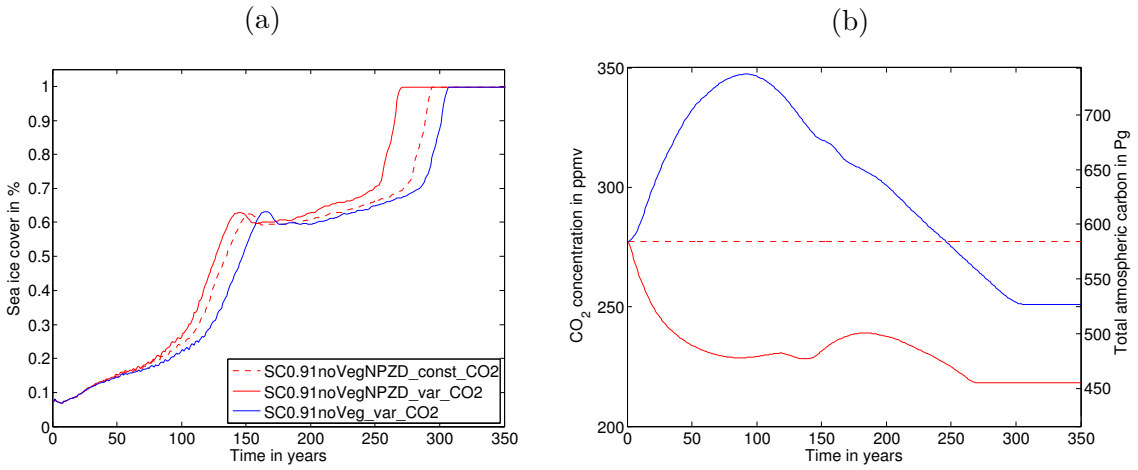

Figure 27: (a) Annual globally averaged sea ice cover in percentage of the global ocean and (b) total atmospheric carbon dioxide concentrationsabsolute carbon content. Red (blue) line denotes the model run without (with) NPZD model.

The focus of this chapter lays on the different processes that change the oceanic outgassing and uptake of carbon dioxide rather than on the effect on the circulation or on the atmospheric and oceanic energy balance. The latter was investigated in the previous two chapters and looks similar for the here investigated SC0.91noVeg_var_CO model run. Figure 28 shows the ocean to atmosphere carbon flux. In comparison to the model run SC0.91noVeg_var_CO, where a net uptake of carbon dioxide due to cooling of the sea surface dominates the carbon flux, the SC0.91noVeg_var_CO simulation shows a net outgassing of carbon dioxide.

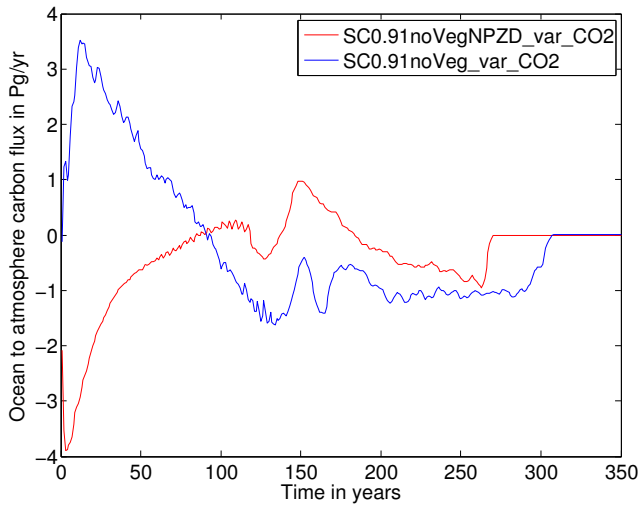

Figure 28: Annual globally averaged ocean to atmosphere carbon flux for the model runs SC0.91noVegNPZD_var_CO2 and SC0.91noVeg_var_CO2

The initial dissolved inorganic carbon (DIC) inventories of the ocean with NPZD module is 3890 Pg larger than for the ocean without the NPZD module. This large amount

of additionally available carbon is stored at medium depth in the tropics and subtropics (see figure 29). The continuous export of detritus into the deep ocean and the remineralisation of detritus due to bacteria, build up this large carbon pool in the sub surface waters. Upwelling and convection are important processes which bring this carbon back to the surface. At the end of the spin up run this upward and downward flux of carbon was in balance, but during the development of Snowball Earth this balance is no more valid.

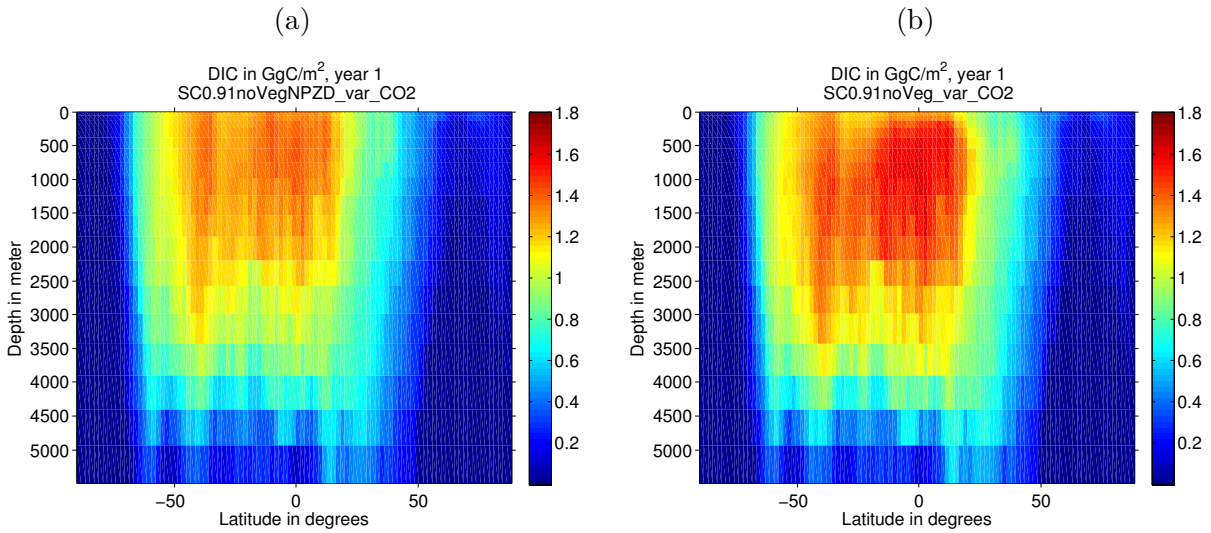

Figure 29: Annual globally integrated oceanic dissolved inorganic carbon (DIC) for model runs (a) SC0.91noVegNPZD_var_CO2 and (b) SC0.91noVeg_var_CO2 at year 1 of the simulations.

The net primary production reduces from 80 PgC/yr to about 35 PgC/yr at the beginning of the simulation and remains below 50 PgC/yr during the whole simulation. A local maximum occurs in year 120 with 46 PgC/yr (see figure 30). The export of carbon due to falling detritus, also shown in figure 30, is ranging from three to zero PgC/yr. The export is strongly coupled to the net primary production, but does not show such a strong decrease at the beginning of the simulation.

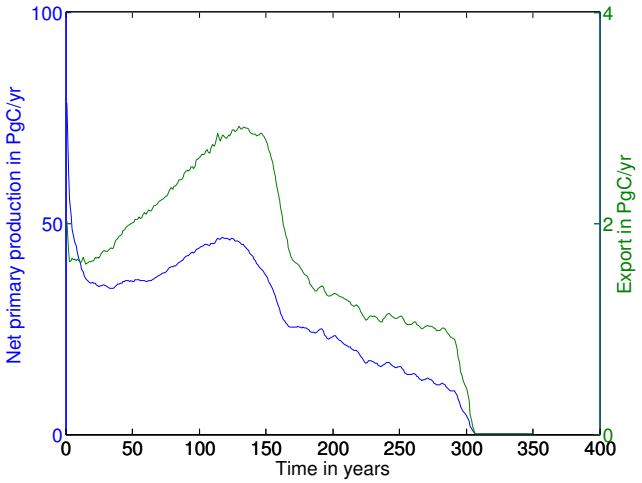

Figure 30: Annual global net primary production for phytoplankton including diazotrophs integrated from the surface to 550 m depth (blue solid line) and the detrital export rate at 643 m (green solid line) for the model run SC0.91noVeg_var_CO2.

Figure 31a shows the rate of change in DIC TgC yr^{-1} m^{-1} for the complete global water column. DIC increases during the first 150 years in the top 1000 meters and decreases in the deep ocean. In the following 150 years the DIC near the surface decreases strongly. Figure 31b shows the rate of change in apparent oxygen utilization (AOU) in terms of carbon to represent the DIC that is formed due to respiration of falling detritus (for simplicity called AOU carbon). At the beginning of the simulation, around 500m depth, strong changes appear in AOU carbon which are caused due to convection (shown later). In the deep ocean the AOU carbon decreases continuously during the first 150 years. It should be noted that conclusions from variations in AOU carbon should not be directly linked to changes in DIC. One can already see in figure 31b that the AOU carbon equivalent overestimates the real changes in DIC. For example convection of water with oxygen under its equilibrium saturation concentration can lead to a decrease of AOU but not necessarily have to lead to an outgassing of the, during the remineralization process formed, carbon dioxide. The decrease in AOU in the deep ocean has to be caused by a perturbation in the biological cycle or by changes in the circulation and convection processes. The global export of detritus shows an increase at this time period which indicates that a lack in detritus is not the reason for the decrease in the deep DIC. Previous model runs show a deepening and enhancement of the tropical circulation cell during the first 150 years (see figure 13) and this model run shows a similar response (not shown). This change in the equatorial circulation can be responsible for the upward transport of additional carbon from the deep that is located not very deep below the surface (see again figure 29).

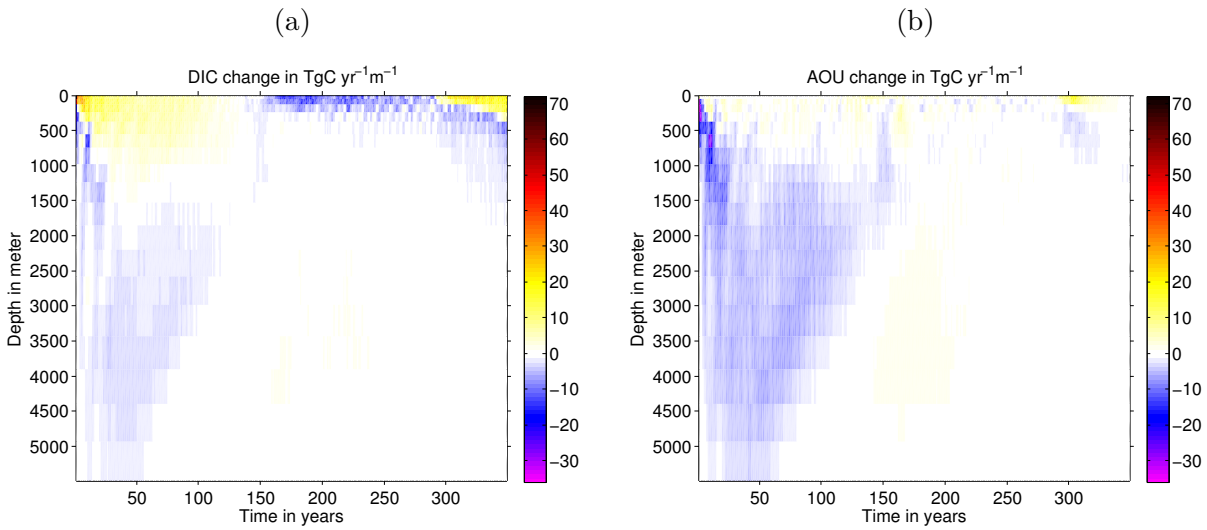

Figure 31: Hovmöller plot for annual values of (a) the change in dissolved inorganic carbon (DIC) and (b) the change in apparent oxygen utilisation (AOU) (both are integrated globally). For the model run SC0.91noVeg_var_CO2.

The absolute AOU (figure 32) reveals more information about the time period between year 150 to year 300. In this time span the AOU carbon below 240m down to the deep ocean increases. Similar to previous model runs this is the time where the freshening event and the warm phase occurs and with this the equatorial circulation is shallowing. The latter allows an accumulation of DIC that is formed due to remineralisation processes. This is one important process that again redistributes the carbon from the surface waters down to the deep ocean.

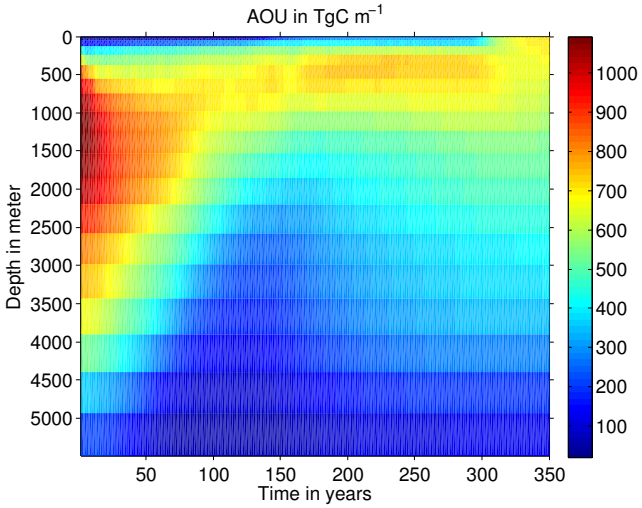

Figure 32: Hovmöller plot for the annual apparent oxygen utilisation (AOU) integrated globally for the model run SC0.91noVeg_var_CO2.

Figure 33a visualizes the redistribution processes of DIC. Shown are changes of the DIC relative to year 1 of the simulation for the deep ocean (blue line) and for the upper

ocean (green line). The net change in oceanic DIC (red line) explains the change in the atmospheric carbon inventory. Organic carbon plays only a minor role for the total budget of DIC. In year 350 the complete organic matter of 10 Pg is transformed into DIC. Figure 33b compares the change in DIC to the change in AOU carbon for the deep ocean since year 150. This figure reveals how important the biological pump during the warming phase is for the removal of DIC from the upper 500m of the ocean.

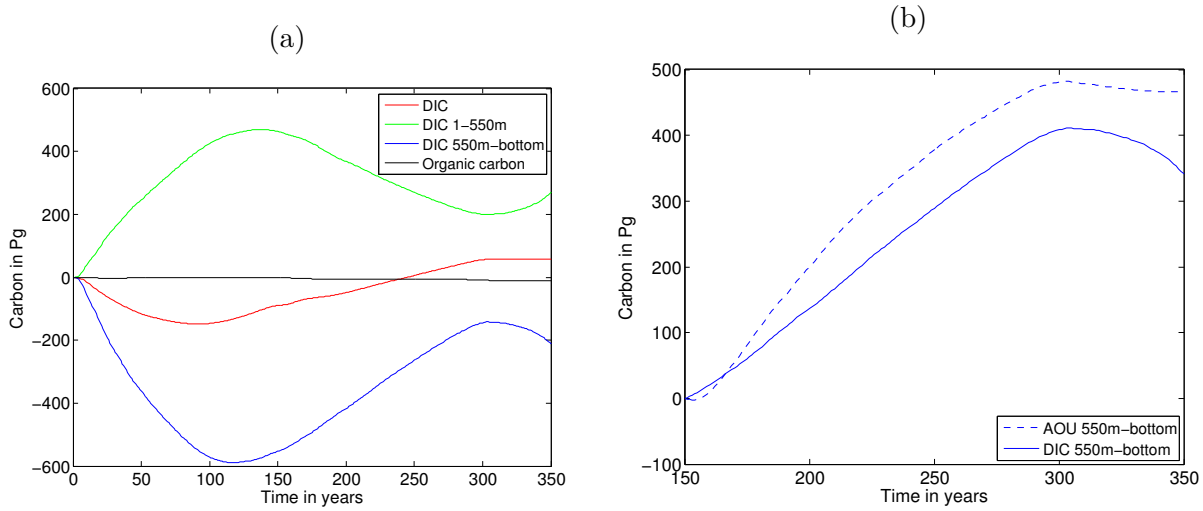

Figure 33: Annual globally integrals of (a) change in global oceanic inventory in dissolved inorganic carbon (DIC) for the whole water column (red line), the upper 550 m (green line) and from 550 m to the bottom (blue line) since year 1. Black line denotes the carbon stored in organic matter. (b) Change in in dissolved inorganic carbon (blue solid line) and in AOU (blue dashed line) in terms of carbon from 550 m to the bottom since year 150. Data from model run SC0.91noVeg_var_CO2.

The meridional distribution of atmosphere to ocean carbon fluxes are shown in figure 34. During the first 150 years the equatorial ocean shows a slight increase in the outgassing of carbon dioxide. This can be due to the change in the equatorial circulation cell, as mentioned above. The subtropics show a net uptake of carbon dioxide and especially in the north subtropics the uptake of carbon dioxide increases. The carbon dioxide flux in the subtropics shows similar patterns to the phytoplankton (see figure 35a). An increase in biological activity also increases the uptake of carbon dioxide. As already shown the export of detritus is enhanced during the first 150 years and reaches its maximum in year 140. This export of organic matter plays an important role for the subtropical waters.

Strong convection appears near the ice edges (see figure 35b) and brings up old, carbon dioxide rich water from below. This causes the strong outgassing near the ice edges. After year 150 the meridional distribution of the sea surface carbon fluxes changes. The equatorial ocean is still outgassing carbon dioxide, but due to the weakening of the equatorial upwelling the flux into the atmosphere reduces. The increase in sea surface temperature

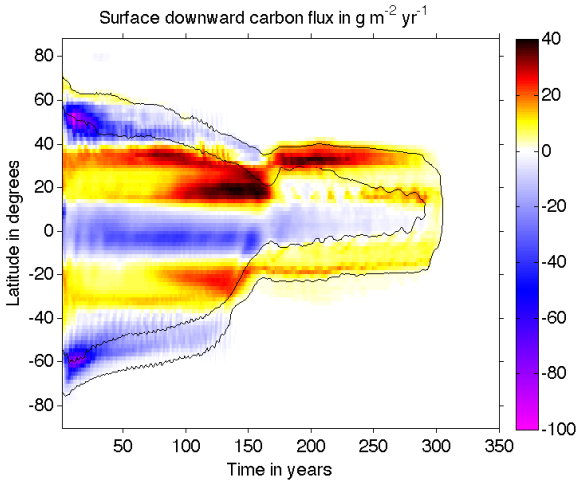

Figure 34: Hovmöller plot of the annual zonal averaged oceanic downward carbon flux for the model run SC0.91noVeg_var_CO2.The inner (outer) black isoline indicates 10% (90%) sea ice cover.

should increase also the equatorial outgassing. The convection activity near the ice edges almost vanishes and the amount of phytoplankton in the upper ocean layer decreases. As the AOU carbon below 550m increases the effectivity of carbon export, due to the biological pump, has to be enhanced. The recirculation of biological matter, due to the shallowing of the equatorial circulation, and the reduction in convection processes have to be reduced. Areas of strong convection only appear in the southern ocean, where the salt brine due to ice formation causes strong vertical convection.

(a) (b)

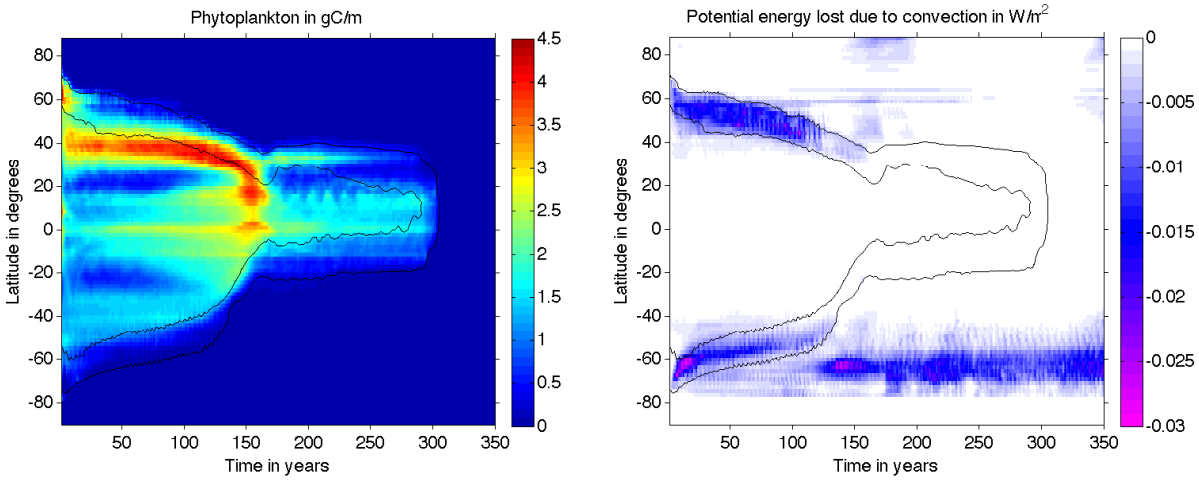

Figure 35: (a) Hovmöller plot of the annual zonal integrated phytoplankton for the upper 550m and (b) Hovmöller plot of the annual potential energy lost due to convection averaged zonally and in time (model run SC0.91noVeg_var_CO2).The inner (outer) black isoline indicates 10% (90%) sea ice cover.

3.2.5 The Land Vegetation

This chapter presents the results of the model run SC0.91noNPZD_var_CO2 including the vegetation model from Meissner et al. (2003), but without marine biogeochemical ecosystem module from Keller et al. (2012). This model run shows similar sea surface temperature (SST) and sea surface salinity (SSS) patterns than previous model runs. The warm phase and the freshening event appear around year 170 and last until year 990 (not shown), the very high level of carbon dioxide extend the warm phase. In year 990 the carbon dioxide concentration reaches 260 ppmv and the greenhouse effect is not strong enough anymore to prevent Snowball Earth (see figure 37). This threshold of 260 ppmv is similar to the threshold that can be found for the SC0.91noVeg_var_CO model run (see figure 27b).

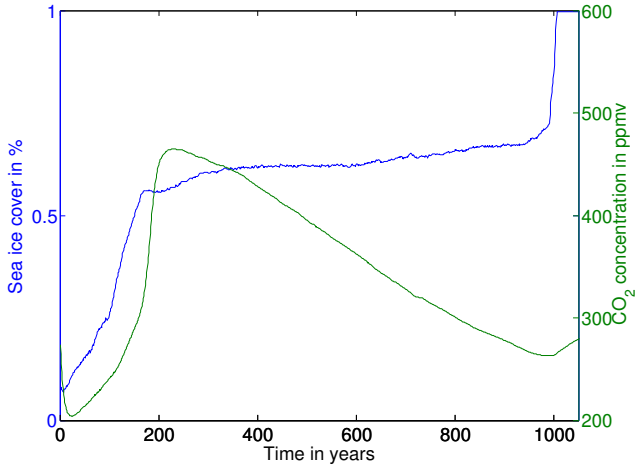

Figure 36: Annual globally averaged sea ice cover (blue solid line) in percentage of the global ocean and total atmospheric carbon dioxide concentration (green solid line) and as carbon content for the model run SC0.91noNPZD_var_CO2.

This model run allows for carbon fluxes between land and atmosphere and for fluxes between ocean and atmosphere (shown in figure 37a), but no carbon flux is possible between land and ocean. At the beginning of the simulation a carbon uptake with nearly 20 Pg/yr appears with an exponential decrease, reaching 0 Pg/yr in year 30. During the first 100 years the land stores 180 Pg carbon, the atmospheric carbon inventory drops by 150 Pg and the ocean outgasses 30 Pg carbon. The solubility for carbon dioxide increases for a cooling ocean and with this the sea surface pCO_2 drops preferring an uptake of carbon dioxide. However the decrease in atmospheric pCO_2 dominates the carbon dioxide air-sea gas exchange and causes an oceanic outgassing of carbon dioxide during the first 45 years. At the beginning of the warm phase in year 183 a peak in the land to atmosphere carbon flux with nearly 15 Pg/yr appears, pushing the atmospheric carbon dioxide concentration to its maximum of 465 ppmv in year 231. From year 231 until the ending of the warm phase in year 990 an ocean uptake of 1.16 ± 0.09 PgC/yr and an

land to atmosphere carbon flux of 0.60 ± 0.23 PgC/yr occurs. The net uptake of carbon decreases the atmospheric carbon dioxide concentration to 260 ppmv in year 990.

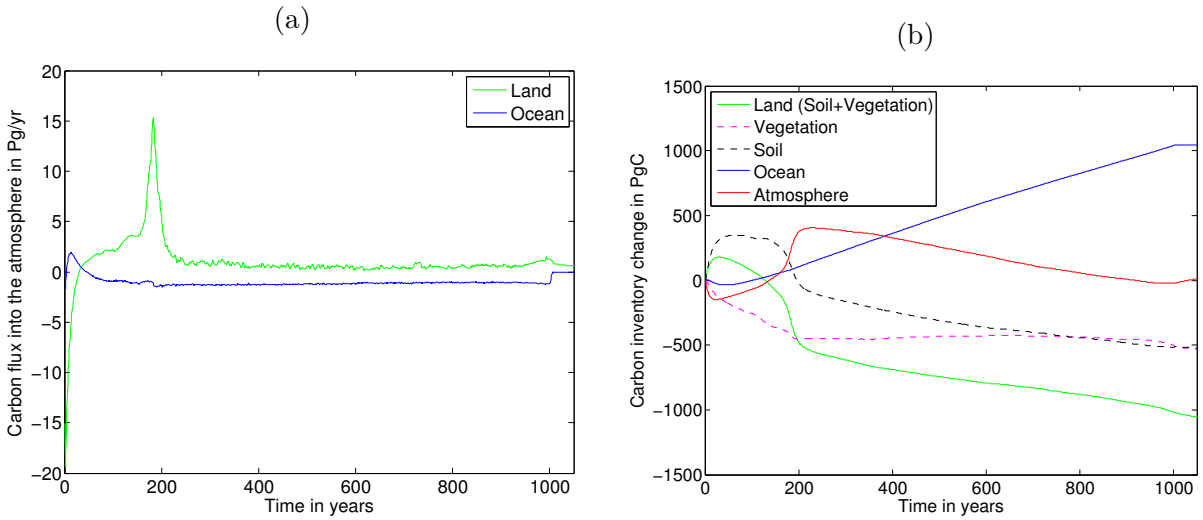

Figure 37: (a) Annual globally averaged carbon fluxes from land/ocean to atmosphere;(b) carbon inventory changes since simulation year 1. Model run SC0.91noNPZD_var_CO2.

The rest of this chapter deals with the land carbon cycle in detail. First I give a short description of the different parameters that are relevant to change the soil and vegetation carbon inventory, a more detailed description can be found in Cox (2001). The land carbon cycle consist of the vegetation carbon pool C_v and the soil carbon pool C_s. The change in the vegetation carbon is described by

$$\frac{dC_v}{dt} = NPP - \Lambda_c \tag{13}$$

with NPP being the net primary production and Λ_c the leaf litter flux. The leaf litter flux depends on turnover rates for the leaf, root and total stem carbon and includes also litter fall due to large-scale disturbance and plant functional type (PFT) competition. The root turnover rate is constant as well as the total steam carbon turnover rate, but the latter depends on the PFT. Broadleaf and needleleaf trees have relatively low turnover rates in comparison to C_3, C_4 grass and shrub. The leaf turnover rate is set to a constant value until the land surface temperature reaches a threshold value, T_{off}. 1°C under this threshold value the leaf turnover rate increases by a factor of 10, for needleleaf trees T_{off} = −30°C and for broadleaf trees T_{off} = 0°C. Hence the leaf litter flux depends on the PFT and on the land surface temperature. The leaf litter flux Λ_c increases the carbon that is stored in the soil. The change in soil carbon is defined by

$$\frac{dC_s}{dt} = \Lambda_c - R_S \tag{14}$$

with R_S the soil respiration. The respiration rate R_S is a function of the carbon content, the soil moisture concentration and the soil temperature. The respiration rate depends linearly on the carbon content C_S. The soil moisture dependence is based on soil moisture optimum value. Below and above this value the respiration rate decreases linearly to some minimum value. The soil temperature dependence is given as an exponential function with $R_S \propto 2^{0.1(T_S-25)}$. The two peaks, that can be seen in the land to atmospheric flux in year 1 and 183, can be explained by the changes in the soil carbon inventory (see figure 37) and therefore the different carbon fluxes for the vegetation and soil inventory are plotted in figure 38. At the end of the spin-up run the soil respiration and the net primary production have to be in equilibrium equal to each other. Already after the first simulation year a difference of 15 PgC/yr appears, peaking in year 2 with nearly 20 PgC/yr.

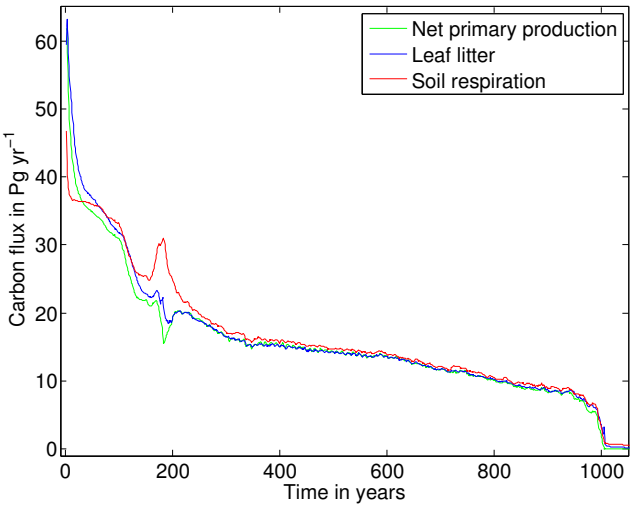

Figure 38: Annual globally averaged sea ice cover (blue solid line) in percentage of the global ocean and total atmospheric carbon dioxide concentration (green solid line) and carbon content for the model run SC0.91noNPZD_var_CO2.

Figure 39 shows global maps for land parameters to analyze in detail why the land peaks so strong during the first year of simulation. Therefore values in figure 39 (c)-(f) are calculated relatively to a reference value, which is defined as the average of the last 10 years of the spin up run. The soil respiration reduces globally almost everywhere (see figure 39c), which is caused by the globally homogeneous decrease in soil temperature (shown in figure 39e). There are also regions that show no decrease in soil respiration. This applies to regions which have generally no carbon stored in the soil, for example North Africa, Australia and regions in the Middle East (compare with figure 39a), or this applies to regions where the soil moisture increases strongly, for example in South East

of North America or in South East of South America (compare with figure 39f). If the soil moisture content is below the optimum value, an increase in soil moisture would also increase the soil respiration, which seems to be the case in the previously named regions. As already shown, the reduction in soil respiration is an important contributor to the global soil carbon content increase.
Another factor is the increase in net primary production in tropical and subtropical regions (see figure 39d). The changing climate has also some positive effect on plant growing. The cooler temperatures seem to reinforce the photosynthesis and moisture stressed plants can benefit from the increase in soil moisture concentration.

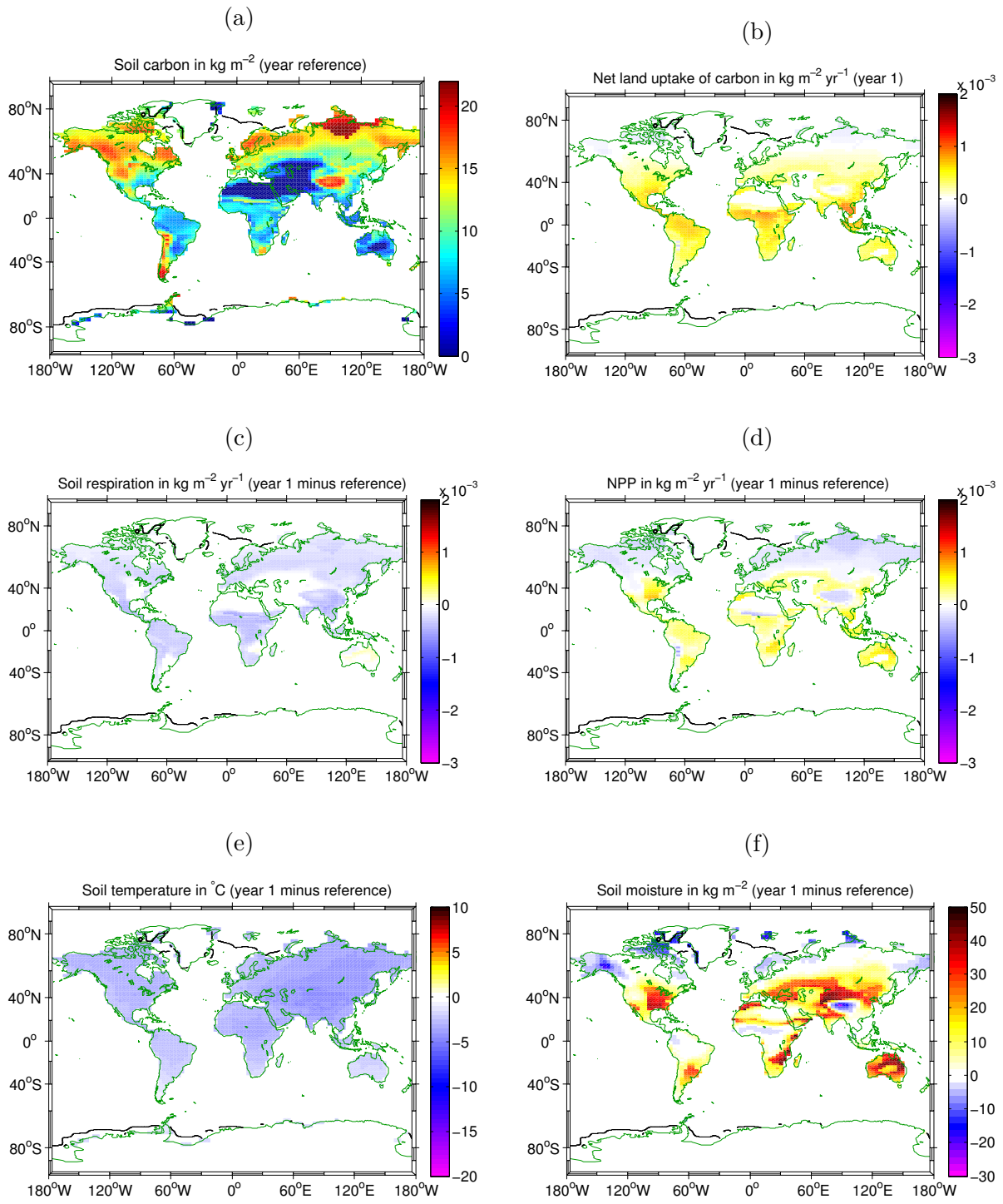

Figure 39: (a) Soil carbon reference inventory. (b) Net land uptake carbon flux (Net primary production (NPP) minus soil respiration) for year 1. Change in (c) soil respiration, (d) NPP, (e) soil temperature and (f) soil moisture. Reference values are calculated from a mean of the last ten years of the spin up run. The black isolines on land (ocean) are lines of 90% sea ice cover (of 1m snow thickness at land). Data from model run SC0.91noNPZD_var_CO2.

Until year 50 one can see already a great redistribution of the soil carbon from the regions of higher latitudes to tropical and subtropical regions (see figure 40a). A weak net land uptake of carbon still occurs in some snow free regions, the snow covered regions generally outgas carbon dioxide (see figure 40b).

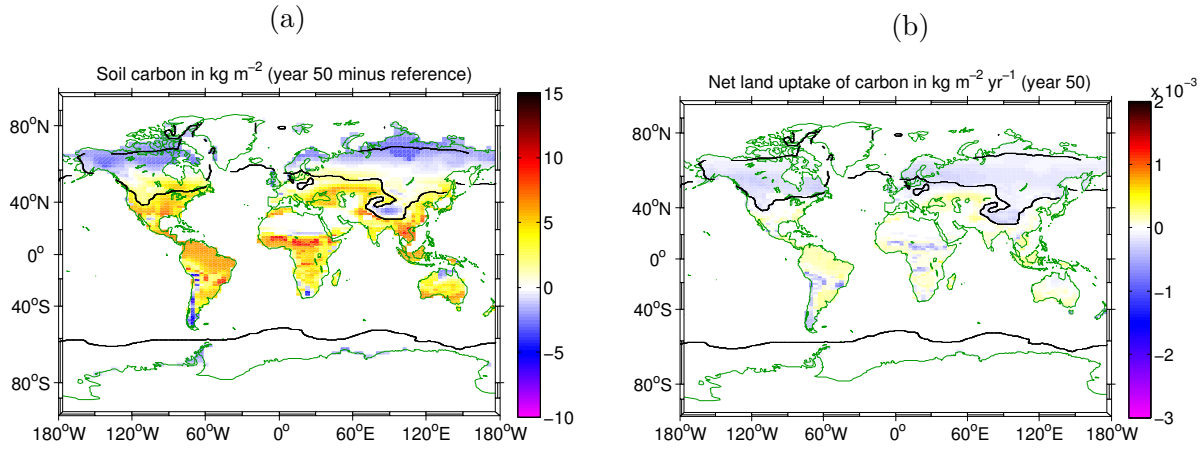

Figure 40: (a) Change in soil carbon inventory for year 50 relative to the reference value. (b) Net land uptake carbon flux (Net primary production (NPP) minus soil respiration) for year 50. Reference values are calculated from a mean of the last ten years of the spin up run. The black isolines on land (ocean) are lines of 90% sea ice cover (of 1m snow thickness at land). Data from model run SC0.91noNPZD_var_CO2.

Until year 183 the accumulation of carbon in the soil of snow free regions has continued and also the loss of soil carbon in snow covered regions (see figure 41a). In this year a peak in the soil to atmosphere carbon flux is mainly driven by the warm phase and the increase in soil respiration. The enhanced soil respiration is driven by very high soil temperatures up to 30 °C (see figure 41c). This strong soil to atmosphere carbon flux is responsible for the peak in atmospheric carbon dioxide concentration of 465 ppmv in year 23 and is also responsible for the long delay of the Snowball Earth development.

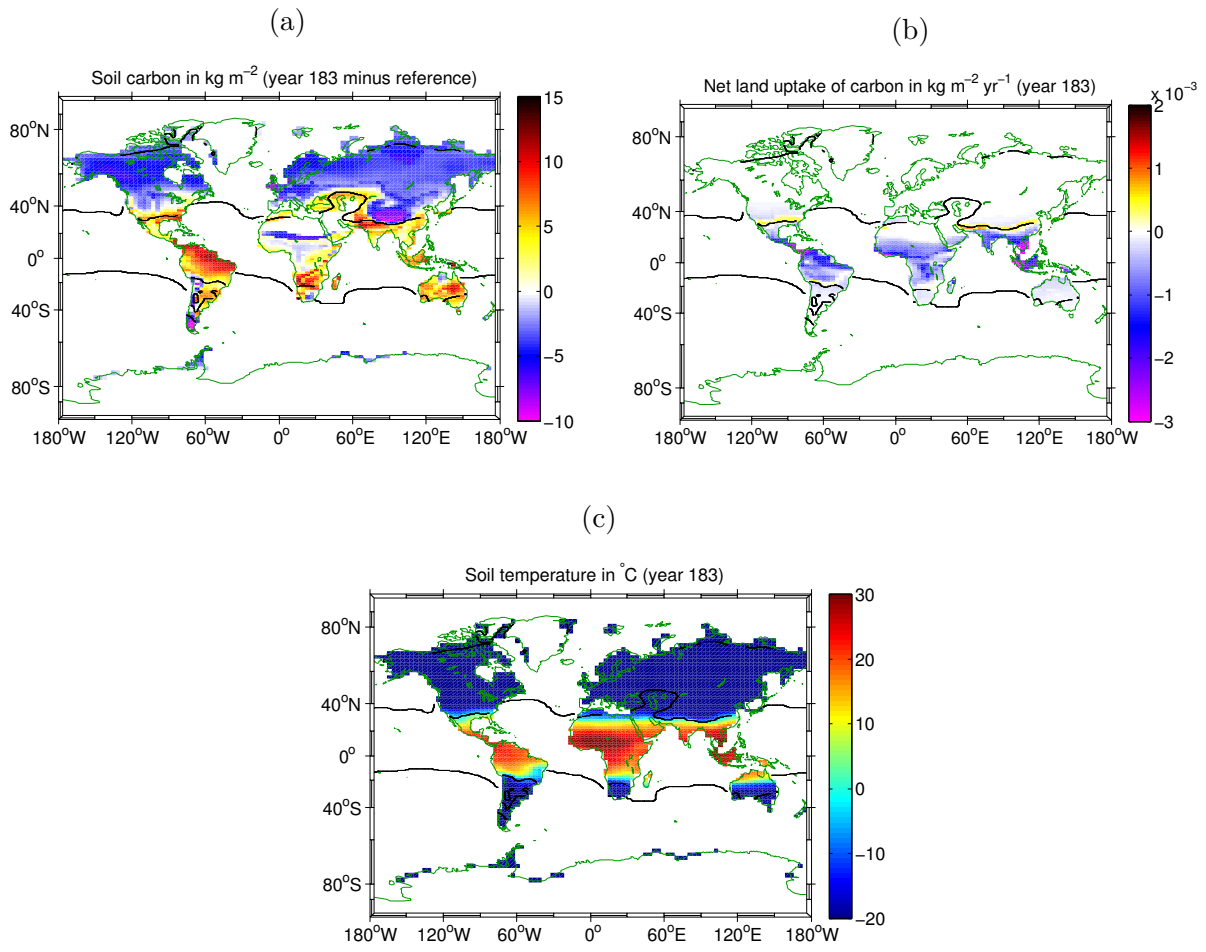

Figure 41: (a) Change in soil carbon inventory for year 183 relative to the reference value. (b) Net land uptake carbon flux (Net primary production (NPP) minus soil respiration) for year 183. (c) Soil temperature for year 183. Reference values are calculated from a mean of the last ten years of the spin up run. The black isolines on land (ocean) indicate lines of 90% sea ice cover (of 1m snow thickness at land). Data from model run SC0.91noNPZD_var_CO2.

3.2.6 Sensitivity to Different Wind Fields

The UVic model is running with a prescribed wind fields. Wind fields contain the wind stress at the sea and land surface and wind velocities relevant for example for atmospheric advection processes and for the latent and sensible heat fluxes. Figure 42 shows the global sea ice cover and the carbon dioxide concentrations for the model runs SC0.91noVegNPZD_const_CO2 and SC0.91_var_CO2 (solid lines) together with two model runs SC0.91_const_CO2_windhalf and SC0.91_var_CO2_windhalf which have the same configuration with exception a reduction of all wind fields to 50% of its initial values. The model runs with weaker wind fields show a less sensitivity to the reduction in incoming solar radiation than the model runs with the standard wind fields. In year 2000 the model run SC0.91_var_CO2_windhalf reaches with 53% global sea ice cover a 5% lower sea ice cover than in the SC0.91_const_CO2_windhalf model run both at similar carbon dioxide concentrations.

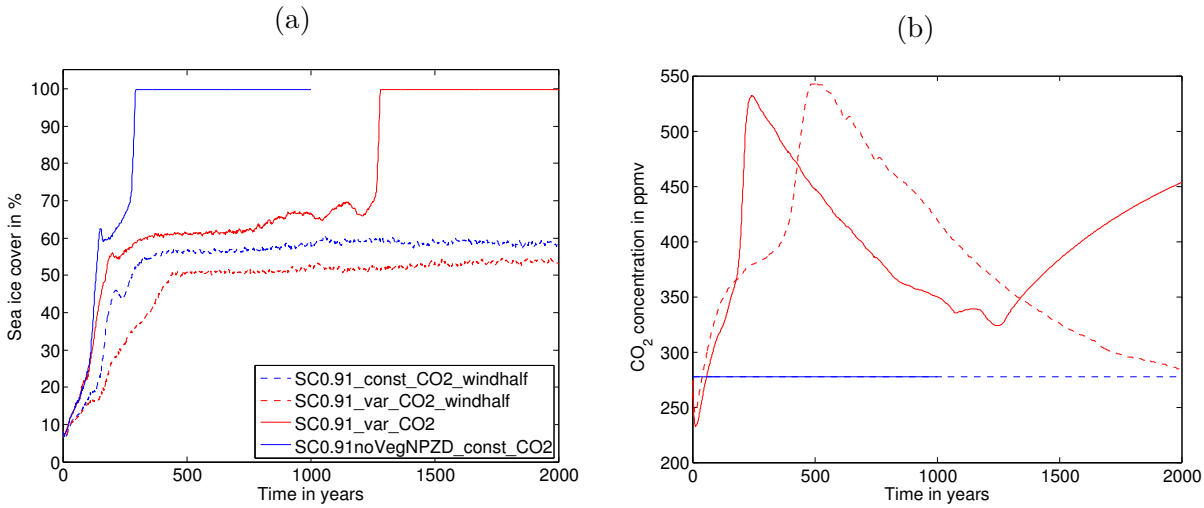

Figure 42: (a) Annual globally averaged sea ice cover in percentage of the global ocean and (b) total atmospheric carbon concentration. Dashed lines denote model runs with modified wind fields.

3.3 Conclusions from Intercomparison with Different Snowball Earth Studies

The bifurcation point for UVic model runs without carbon cycle is between 91% and 94% of present day incoming solar radiation (PDISR), which is similar to the results with the coupled atmosphere-ocean general circulation model ECHAM5/MPI-OM (Voigt and Marotzke, 2009). Yang et al. (2012a) used the Community Climate System Model (CCSM3) and preindustrial carbon dioxide concentration. In their study the bifurcation point is between 10% and 10.5% PDISR. The latter model run was carried out with a sea ice albedo of 0.5 which is much lower than the sea ice albedo of 0.75 that were used in this study and in the study by Voigt and Marotzke (2009). Yang et al. (2012a) performed also a model run with a sea ice albedo of 0.75 and 94% PDISR, but in this model run a Snowball Earth state is reached in contrast to the corresponding UVic model runs.
The transition times in the UVic model are generally shorter than in the CCSM3 or in ECHAM5/MPI-OM model. For example the transition time is 128 years with the UVIC model (87% incoming solar radiation), 285 years with the ECHAM5/MPI-OM model (87% incoming solar radiation) and around 220 years with the CCSM3 model (88% incoming solar radiation). Yang et al. (2012b) stated that changes in the atmospheric circulation and the wind-driven ocean circulation play an important role to delay the expansion of sea ice into the tropics, this response in the wind fields cannot be simulated with the UVic model and could be responsible for the shorter transition times.
Yang et al. (2012b) and Voigt and Marotzke (2009) observe a strengthening of the southern Hadley Cell and the tropical wind-drive circulation at the point the sea ice starts to expand to the tropical ocean. In UVic model runs an increase in the meridional temperature gradient and a reduction in poleward heat transport can be observed. With the stronger equator-to-pole temperature gradient a strengthening of the atmospheric poleward heat transport would be expected as observed by Voigt and Marotzke (2009), but due to the missing atmospheric response in the UVic model the tropical atmospheric temperature further increases and the warm phase develops though. As the sea ice expands to the tropics the equatorward latent heat transport due to sea ice increases strongly and the melting of the sea ice reduces the tropical sea surface salinity. The sea surface freshening supports the development of the warming phase as it increases the vertical density gradient and with this the mixing. A strengthening of the southern Hadley Cell and the tropical wind-driven circulation would inhibit the expansion of sea ice into the tropics (Yang et al., 2012b) and would also influence the freshening of the tropical open ocean regions in the UVic model runs. More detailed investigations are necessary to determine the influences of changes in atmospheric circulations in the UVic model and to identify the uncertainties which arise from prescribing the wind fields in the UVic model.
Despite this and the problem with prescribed wind fields this study shows that the marine

and land carbon cycle already reacts very fast during the development of the Snowball Earth with almost a doubling of the atmospheric carbon dioxide concentration. A large part of the atmospheric carbon dioxide concentration rise results from the land to atmosphere carbon flux during the warm phase. Further investigation with a full complex atmospheric/ocean general circulation model and a land and ocean carbon cycle should reveal if this warm phase and the simultaneous increase in soil respiration are meaningful or more an artifact of the missing atmospheric feedbacks.

Yang et al. (2012b) stated that the most relevant feedbacks for promoting global sea ice cover are the water vapor feedback and the ice albedo feedback. They also mentioned the changes in the different forcing for an experiment with 6% less solar radiation and 70 ppmv in carbon dioxide concentration: The strongest reduction is given with -54.4 W/m^2 in the water vapor greenhouse effect and with -22.4 W/m^2 in the absorbed solar radiation. The global forcing due to the oceanic and atmospheric heat transport strengthen with 16.3 and 6.2 W/m^2. The UVic model can simulate changes in the water vapor greenhouse effect, in the reflection of shortwave radiation due to a varying surface albedo and in the oceanic heat transport, but UVic not correctly simulates changes in the atmospheric heat transport. The above mentioned simulation from Yang et al. (2012b) are not directly comparable to the simulations done in this study, but one could expect that an additional cooling due to the atmospheric heat transport of the above mentioned 6.2 W/m^2 are not negligible in comparison to the dynamic greenhouse forcing that is ranging for the experiments in this study from -1 to 3.4W/m^2.

The wind sensitivity test in chapter 3.2.6 reveals the strong influence of the wind on the development of a Snowball Earth. This test also shows an interesting influence of the carbon cycle as a side aspect. At year 2000 in model run SC0.91_const_CO2_windhalf and SC0.91_var_CO2_windhalf both models reach a similar carbon dioxide concentration, but a global sea ice cover difference of 5% remains. This difference have to be due to the influence of the dynamic carbon cycle and it would need further investigation why this effect is still identifiable in year 2000.

The UVic model does not account for the effect of clouds on the long and shortwave radiation and uses a prescribed atmospheric albedo mask instead to simulate a reflection of short wave radiation at the top of the atmosphere for a present day climate. Voigt and Marotzke (2009) found that the effect of clouds on the planetary albedo is changing and reducing during the development of a Snowball Earth. One could investigate UVic model runs with different atmospheric albedo masks to reduce and estimate the uncertainties that arise from cloud effects.

Dust accumulation on sea ice reduces the amount of atmospheric carbon dioxide that is necessary for deglaciation (Goodman and Strom, 2013). The investigation of the effect of dust accumulation at sea ice during the development of a Snowball Earth or a changing sea ice albedo accounting for the sea ice aging process can be part of further investiga-

tions.
Simulation SC0.91noNPZD_var_CO2 reveals growing vegetation in tropical regions during the first 100 years and with this a change in land surface albedo. Further investigation are needed to determine the role of this and other land albedo changes for the development of a Snowball Earth.

4 Summary

Using the modified UVic model with a present day continent distribution, this study examined the relevant processes that appear during the development of a modern Snowball Earth focussing on the limitations of the atmospheric model and on carbon cycle feedbacks.

First the UVic reference model run without carbon cycle (SC0.91noVegNPZD_const_CO2) is compared to model runs of the full-complex ECHAM5/MPI-OM (Voigt and Marotzke, 2009). The comparison reveals an accordance in the bifurcation point laying between 91% and 94% of the present-day solar constant and differences in the transition time, showing a shorter transition time in the UVic model. UVic model runs show the appearance of a warm phase when the sea ice begins to expand towards tropical regions. This warm phase is not observed in modern Snowball Earth studies with coupled atmosphere-ocean general circulation models (Voigt and Marotzke, 2009; Yang et al., 2012a). The main driver of the warm phase is a decrease in atmospheric heat transport into the tropics as the sea ice reaches tropical waters. The consequence of this is an increase in the atmospheric meridional temperature gradient. Voigt and Marotzke (2009) and Yang et al. (2012a) observed a simultaneous strengthening of the atmospheric circulation and of the wind driven ocean circulation increasing the poleward heat transport. The UVic atmospheric model has a prescribed wind field and therefore shows no response in the circulation strength. The temperature difference between atmosphere and ocean is identified to increase sensible heat fluxes warming the tropical ocean surface waters. The ocean circulation reacts to the increase of ocean surface temperatures with a cooling of the sea surface due to changes in the vertical and horizontal advection. At the same time the equatorward expansion of sea ice is stopped and sea ice is melts near the sea ice edges, which is freshening the surface waters. Both the freshening and the warming reduce the sea surface density and increase the vertical density gradient of the water column near the surface. The increase in the vertical density gradient is responsible for a shallowing of the tropical meridional overturning circulation and also reduces the cooling due to the vertical advection of cold water from below, establishing the warm phase. The sea ice is formed in polar regions in the southern hemisphere where strong convection appears due to the salt brine release.

The duration of the warm phase is very sensitive to the greenhouse forcing due to changes in the carbon dioxide concentration. The forcing ranges from -1.8 to 3.4 W/m^2 relative to the preindustrial forcing. Figure 43 shows summary plots for sea ice cover, carbon dioxide concentrations and the atmospheric forcing of the different model configurations which are used in this study to investigate the influence of the carbon cycle. In the following the findings from the model runs with dynamic carbon cycle are summarized.

The model run with a dynamic atmospheric carbon pool (SC0.91noVegNPZD_var_CO2) reveals the effect of the solubility pump. The net effect is a is shortening of the transition

time by 24 years. During the first 50 years the greenhouse forcing due to carbon dioxide reduces by 1.4W/m^2 and during the warm phase an oceanic outgassing of carbon dioxide can be observed.

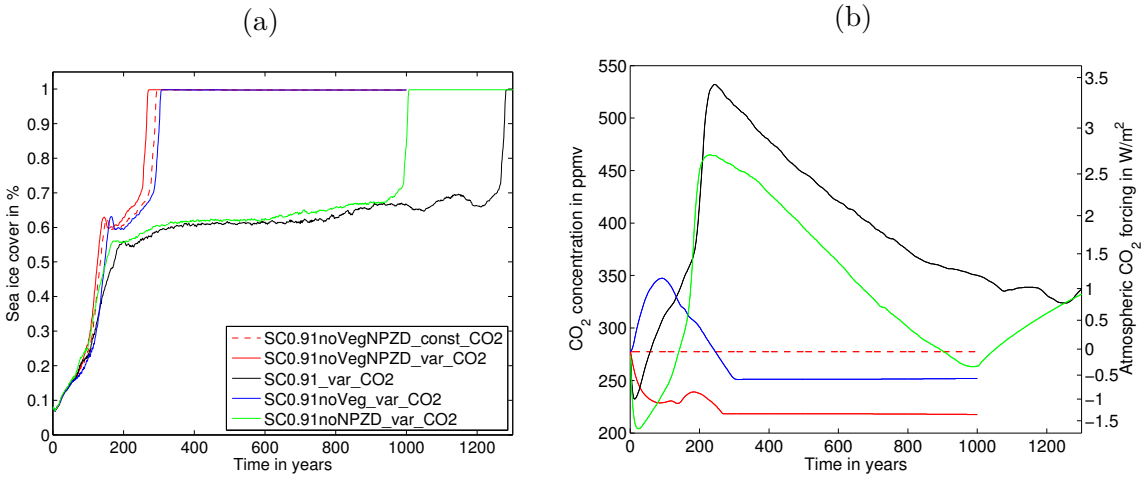

Figure 43: (a) Annuall globally averaged sea ice cover in percentage of the global ocean and (b) total atmospheric carbon dioxide concentrations in ppmv and the respective atmospheric greenhouse forcing anomaly relative to the preindustrial forcing. Solar irradiance is set at the beginning at fixed 91% PSC.

The marine ecosystem is simulated with a NPZD model in the SC0.91noVeg_var_CO2 model run. During the first 150 years an outgassing of 150 Pg carbon occurs, delaying Snowball Earth for 12 years in comparison to the reference run. The initial carbon concentration in the ocean below the mixed layer is higher than of the surface water due to the remineralisation process of detritus or with other words due to the biological pump. Strong convection processes and the enhancement of the meridional overturning circulation during the first 150 years bring this carbon up to the surface. Due to the pressure effect on the carbon dioxide solubility, the solubility decreases at the sea surface and a large amount of carbon dioxide gasses out. The pressure effect on the solubility is here more important than the increase in solubility due to the cooling of the ocean. During the warm phase carbon is removed from the surface water due to the export of detritus and stored in the waters below 550 m, what was concluded from the increase in the apparent oxygen utilization. The shallowing of the equatorial circulation and the reduced convection activity reduced the recirculation of organic carbon to the mixed layer. During the warm phase the carbon dioxide concentration is reduced to 251ppmv.
The influence of the vegetation on the carbon fluxes is investigated with the SC0.91noNPZD_var_CO2 model run. In the first years of the simulation the vegetation responds very fast on the temperature drop with a net uptake of carbon dioxide. The soil respiration reduces immediately as the soil temperature drops and the carbon

accumulates in the soil. The decrease in land temperature improves the condition for plant growth in tropical and subtropical regions. This is also responsible for the global positive net primary production. In regions of the northern boreal forests the cooling temperatures are responsible for the decrease in local land carbon. During the first 50 years a large amount of carbon is stored in tropical and subtropical regions which are then again outgassed during the warm phase due to enhanced soil respiration. In the UVic vegetation model soil temperature and soil respiration are strongly coupled. In the warm phase the solubility pump is the main driving force for the reduction in the atmospheric carbon dioxide concentration and allows Snowball Earth state to be reached.
Model run SC0.91_var_CO2 is not investigated in this study. Table 6 gives a short summary about the Snowball Earth transition times and the final carbon dioxide concentrations when a Snowball Earth state is reached. The SC0.91_var_CO2 model run has a transition phase that is more than 250 years longer than the model run with vegetation. Additional investigations are necessary to identify feedbacks between the land and marine carbon cycle.
However this study shows that the response time of the marine and land carbon cycle are fast enough to show an important impact during the development of a Snowball Earth. Strong enough to counter the effect of the solubility pump for a certain time span.

Table 6: Year of Snowball Earth (SE) development and the respective atmospheric carbon dioxide concentration.

Simulation	CO_2 in ppmv	reaching SE in years
SC0.91noVegNPZD_const_CO2	277	295
SC0.91noVegNPZD_var_CO2	218	271
SC0.91noVeg_var_CO2	251	307
SC0.91noNPZD_var_CO2	265	1007
SC0.91_var_CO2	330	1282

References

Cox, P. M., 2001: Descrition of the 'TRIFFID' dynamic global vegetation model. Tech. rep., Hadley Centre Technical Note 24, 1–16 pp.

Eby, M., K. Zickfeld, A. Montenegro, D. Archer, K. J. Meissner, and A. J. Weaver, 2009: Lifetime of Anthropogenic Climate Change: Millennial Time Scales of Potential CO 2 and Surface Temperature Perturbations. *Journal of Climate*, **22 (10)**, 2501–2511, doi:10.1175/2008JCLI2554.1.

Eby, M., et al., 2013: Historical and idealized climate model experiments: an intercomparison of Earth system models of intermediate complexity. *Climate of the Past*, **9 (3)**, 1111–1140, doi:10.5194/cp-9-1111-2013.

Fanning, A. F. and A. J. Weaver, 1996: An atmospheric energy-moisture balance model: Climatology, interpentadal climate change, and coupling to an ocean general circulation model. *Journal of Geophysical Research*, **101 (D10)**, 15 111, doi:10.1029/96JD01017.

Getzlaff, J. and H. Dietze, 2013: Effects of increased isopycnal diffusivity mimicking the unresolved equatorial intermediate current system in an earth system climate model. *Geophysical Research Letters*, **40 (10)**, 2166–2170, doi:10.1002/grl.50419.

Goodman, J. C. and D. C. Strom, 2013: Feedbacks in a coupled ice-atmosphere-dust model of the glacial Neoproterozoic "Mudball Earth". *Journal of Geophysical Research: Atmospheres*, **118 (20)**, 11,546–11,557, doi:10.1002/jgrd.50849.

Keller, D. P., A. Oschlies, and M. Eby, 2012: A new marine ecosystem model for the University of Victoria Earth System Climate Model. *Geoscientific Model Development*, **5 (5)**, 1195–1220, doi:10.5194/gmd-5-1195-2012.

Kirschvink, J. L., 1992: Late Proterozoic low-latitude global glaciation: the snowball Earth. *The Proterozoic Biosphere*, Schopf & Klein, Vol. 52, 51–52.

Lewis, J. P., a. J. Weaver, and M. Eby, 2006: Deglaciating the snowball Earth: Sensitivity to surface albedo. *Geophysical Research Letters*, **33 (23)**, L23 604, doi: 10.1029/2006GL027774.

Lewis, J. P., A. J. Weaver, and M. Eby, 2007: Snowball versus slushball Earth: Dynamic versus nondynamic sea ice? *Journal of Geophysical Research*, **112 (C11)**, C11 014, doi:10.1029/2006JC004037.

Meissner, K. J., A. J. Weaver, H. D. Matthews, and P. M. Cox, 2003: The role of land surface dynamics in glacial inception: a study with the UVic Earth System Model. *Climate Dynamics*, **21 (7-8)**, 515–537, doi:10.1007/s00382-003-0352-2.

Pierrehumbert, R. T., 2005: Climate dynamics of a hard snowball Earth. *Journal of Geophysical Research*, **110 (D1)**, D01 111, doi:10.1029/2004JD005162.

Thompson, S. L. and S. G. Warren, 1982: Parameterization of Outgoing Infrared Radiation Derived from Detailed Radiative Calculations. *Journal of the Atmospheric Sciences*, **39 (12)**, 2667–2680, doi:10.1175/1520-0469(1982)039<2667:POOIRD>2.0.CO;2.

Trenberth, K. E., J. T. Fasullo, and J. Kiehl, 2009: Earth's Global Energy Budget. *Bulletin of the American Meteorological Society*, **90 (3)**, 311–323, doi:10.1175/2008BAMS2634.1.

Voigt, A. and D. S. Abbot, 2012: Sea-ice dynamics strongly promote Snowball Earth initiation and destabilize tropical sea-ice margins. *Climate of the Past*, **8 (6)**, 2079–2092, doi:10.5194/cp-8-2079-2012.

Voigt, A., D. S. Abbot, R. T. Pierrehumbert, and J. Marotzke, 2011: Initiation of a Marinoan Snowball Earth in a state-of-the-art atmosphere-ocean general circulation model. *Climate of the Past*, **7 (1)**, 249–263, doi:10.5194/cp-7-249-2011.

Voigt, A. and J. Marotzke, 2009: The transition from the present-day climate to a modern Snowball Earth. *Climate Dynamics*, **35 (5)**, 887–905, doi:10.1007/s00382-009-0633-5.

Weaver, A. J., et al., 2001: The UVic earth system climate model: Model description, climatology, and applications to past, present and future climates. *Atmosphere-Ocean*, **39 (4)**, 361–428, doi:10.1080/07055900.2001.9649686.

Yang, J., W. R. Peltier, and Y. Hu, 2012a: The Initiation of Modern "Soft Snowball" and "Hard Snowball" Climates in CCSM3. Part I: The Influences of Solar Luminosity, CO 2 Concentration, and the Sea Ice/Snow Albedo Parameterization. *Journal of Climate*, **25 (8)**, 2711–2736, doi:10.1175/JCLI-D-11-00189.1.

Yang, J., W. R. Peltier, and Y. Hu, 2012b: The Initiation of Modern "Soft Snowball" and "Hard Snowball" Climates in CCSM3. Part II: Climate Dynamic Feedbacks. *Journal of Climate*, **25 (8)**, 2737–2754, doi:10.1175/JCLI-D-11-00190.1.

Acknowledgement

I would like to thank Andreas Oschlies and David Keller for supervising me and for guiding and supporting me during the completion of the thesis. Also, I am grateful to Michael Urban, Julia Errens, Markus Graemer, Svenja Ryan, Anja Sendelbeck and Siren Rühs for their helpful comments and suggestions, and to Janine Urban for supporting me over the whole thesis.

Erklärung

Ich versichere, dass ich meine Master Thesis mit dem Titel *Impact of the carbon cycle on the development of a Snowball Earth* selbständig und ohne Benutzung anderer als der angegebenen Hilfsmittel angefertigt habe. Die Arbeit hat bisher in gleicher oder ähnlicher Form oder auszugsweise noch keiner Prüfungsbehörde vorgelegen.

Kiel, den 09.04.2014

(Tronje Peer Kemena)